Contributions to Mineralogy and Petrology (2019) 174:79
https://doi.org/10.1007/s00410-019-1609-z

ORIGINAL PAPER

Oxygen fugacity at the base of the Talkeetna arc, Alaska

Claire E. Bucholz[1] · **Peter B. Kelemen**[2]

Received: 12 March 2019 / Accepted: 2 August 2019

Abstract

The origin of the more oxidized nature of arc magmas as compared to that of mid-ocean ridge basalts (MORB) is debated, considered to be either a feature of their mantle source, or produced during crustal transit and eruption. Fe^{3+}/Fe^{T} ratios ($Fe^{3+}/[Fe^{3+}+Fe^{2+}]$) in arc volcanic rocks and glasses and thermodynamic oxybarometry on mantle xenoliths from arc lavas indicate elevated magmatic oxygen fugacity (f_{O_2}), whereas, redox-sensitive trace elements ratios and abundances in arc volcanic rocks have been used to suggest that arcs have source regions with f_{O_2} similar to the MORB source. Here, we take an alternative approach by calculating the f_{O_2} of the uppermost mantle and lowermost ultramafic cumulates from the accreted Jurassic Talkeetna arc (Alaska). This approach allows us to quantify the f_{O_2} of the sub-arc mantle and of primary arc magmas crystallizing at the base of an island arc, which have not been affected by processes during crustal transit and eruption which could affect their f_{O_2}. Implementing olivine–spinel oxybarometry, we find that the upper mantle (harzburgites and lherzolites) and ultramafic cumulates (clinopyroxenites and dunites) crystallized between +0.4 and +2.3 log units above the fayalite-magnetite-quartz buffer, consistent with previous studies suggesting that the sub-arc mantle is oxidized relative to that of MORB. In addition, the Talkeetna paleo-arc allows us to examine coeval lavas and their redox-sensitive trace element ratios (e.g., V/Sc). The average V/Sc ratios of high MgO (> 6 wt%) lavas are 6.7 ± 1.6 (2σ), similar to that of MORB. However, V/Sc ratios must be interpretted in terms the degree of partial melting, as well as, the initial V/Sc ratio of the mantle source in order to derive information about f_{O_2} of their mantle source. The V/Sc ratios of Talkeetna lavas are consistent with the elevated f_{O_2} recorded in the sub-arc mantle and primitive cumulates (olivine Mg# [Mg/(Mg + Fe)] × 100 > 82) if a depleted mantle source underwent 15–20% melting. Our results suggest that the arc mantle is, on average, more oxidized than the MORB source and that V/Sc ratios must be interpreted in the context of a partial melting model where all model parameters are appropriate for arc magma genesis. This study reconciles V/Sc ratios in arc volcanic rocks with f_{O_2} of primary arc basalts and the sub-arc mantle from the same locality.

Keywords Oxygen fugacity · Cumulate · Island arc · Talkeetna

Introduction

It has long been recognized that there is significant variability in the oxygen fugacity (f_{O_2}) of magmas from different tectonic settings (e.g., Osborn 1959; Wood 1990; Carmichael 1991; Arculus 1994; Lee et al. 2005; Kelley and Cottrell 2009; Evans et al. 2012). Mid-ocean ridge basalts (MORB) are characterized by a narrow range of f_{O_2} values near the fayalite–magnetite–quartz (FMQ) buffer or approximately one log unit below the Ni–NiO buffer (NNO) (Christie et al. 1986; Bézos and Humler 2005; Cottrell and Kelley 2011; Kelley and Cottrell 2012; Berry et al. 2018; Zhang et al. 2018), whereas arc volcanic rocks are characterized by higher and more variable f_{O_2}, 0.5–3.5 log units higher than FMQ (FMQ + 0.5 to + 3.5; Carmichael 1991; Sisson

Communicated by Timothy L. Grove.

Electronic supplementary material The online version of this article (https://doi.org/10.1007/s00410-019-1609-z) contains supplementary material, which is available to authorized users.

✉ Claire E. Bucholz
cbucholz@caltech.edu

[1] Division of Geological and Planetary Sciences, California Institute of Technology, 1200 E California Boulevard, Pasadena, CA 91125, USA

[2] Lamont-Doherty Earth Observatory, Columbia University, Palisades, NY 10964, USA

Published online: 09 September 2019

et al. 2005; Kelley and Cottrell 2009; Brounce et al. 2014; Richards 2015). f_{O_2} in arc magmatic rocks has been determined using five approaches: (1) thermodynamic assessment of mineral equilibria in volcanic rocks (e.g., Evans et al. 2012); (2) measurement of Fe^{3+}/Fe^{T} ratios in volcanic rocks, glasses, or melt inclusions (e.g., Carmichael 1991; Kelley and Cottrell 2009; Brounce et al. 2014); (3) olivine–orthopyroxene–spinel oxybarometry of supra-subduction zone peridotite xenoliths (e.g., Parkinson and Pearce 1998; Parkinson and Arculus 1999); (4) mineral equilibria in gabbroic rocks from the arc lower crust (Behn and Kelemen 2006); and (5) redox-sensitive element ratios and abundances (e.g., V/Sc: Li and Lee 2004; Lee et al. 2005; Fe^{T}/Zn: Lee et al. 2010; Cu: Lee et al. 2012; and V/Yb: Laubier et al. 2014). The first four methods broadly suggest that both arc magmas and their sub-arc mantle source regions are oxidized relative to MORB. For example, Fe^{3+}/Fe^{T} ratios in olivine-hosted melt inclusions from arcs are 0.18–0.32, corresponding to f_{O_2} greater than FMQ + 1 (Kelley and Cottrell 2009; Brounce et al. 2014), whereas those of MORB glasses are 0.14 ± 0.01 corresponding to f_{O_2} values of FMQ − 0.18 ± 0.16 (Zhang et al. 2018). Similarly, the majority of supra-subduction zone peridotite xenoliths record f_{O_2} between FMQ + 0.5 and FMQ + 2.5 (see Richards 2015 for compilation) and mineral assemblages in arc gabbronorites indicate equilibration at $f_{O_2} >$ FMQ + 2 (Behn and Kelemen 2006). These elevated f_{O_2} values are commonly ascribed to the mass transfer of volatiles and/or oxidized species in hydrous fluids or melts from the subducting slab into the mantle wedge, where arc magmas are generated (Canil et al. 1994; Brandon and Draper 1996; Parkinson and Arculus 1999; Kelley and Cottrell 2009; Brounce et al. 2014). In contrast, redox-sensitive trace element ratios and Fe isotopes have been used to suggest that the f_{O_2} of the mantle source region of arc magmas is similar to that of MORB (i.e., near FMQ) and that the elevated f_{O_2} of arc lavas arises due to subsequent crustal processes, such as crystal fractionation, assimilation of oxidized material, and degassing (Lee et al. 2005, 2010, 2012; Dauphas et al. 2009; Mallmann and O'Neill 2009; Tang et al. 2018). (However, see Laubier et al. 2014 for interpretation of V/Yb ratios as evidence for a heterogeneous and, on average, more oxidized source region for arc magmas.)

Distinguishing between the hypotheses above that the observed elevated f_{O_2} in arc volcanic rocks is (A) inherited from the mantle wedge or (B) produced by crustal processes is complicated using the volcanic record. This difficulty arises because the composition of lava is the result of a potentially complex magmatic history, combining both source region characteristics and the effects of subsequent crustal processes. A critical, yet relatively understudied archive of f_{O_2} in arc magmatism is in primitive cumulates. These represent the first products of crystallizing, primitive arc lavas, which have not experienced subsequent crustal processes (e.g., extensive crystal fractionation, degassing, or assimilation) that could have modified their f_{O_2}. For example, Tang et al. (2018) calculated the f_{O_2} of garnet pyroxenite cumulate xenoliths from a Late Cretaceous to Early Paleogene continental arc (Arizona, USA) using Eu anomalies in clinopyroxene and garnet. They found that the most primitive cumulates initially crystallized near the FMQ − 1 (± 1 log unit) and that the f_{O_2} increased during crystallization due to fractionation of Fe^{2+}-rich garnet. Another example is the study of Behn and Kelemen (2006), building on the work of Lindsley and Frost (1992), showing that the mineral assemblage in gabbronorites from the Talkeetna arc—whole rock Mg# of 58, without olivine, garnet, or quartz—is only stable at an f_{O_2} greater than FMQ + 2. However, a similar test has not been done using thermodynamically based olivine–spinel oxybarometry on primitive cumulates from an oceanic arc.

Here, we present calculations on the f_{O_2} of the uppermost mantle and lowermost primitive (olivine Mg# > 82), ultramafic cumulates from the accreted, Jurassic Talkeetna arc in south-central Alaska using olivine–spinel oxybarometry. The Talkeetna paleo-arc is a "type" locality for a relatively complete accreted oceanic arc preserving rocks from the petrologic Moho to volcanic rocks. In addition, it has been extensively studied over the last 30–40 years (Burns 1985, Burns et al. 1991; Newberry et al. 1986; DeBari and Coleman 1989; Plafker et al. 1989; DeBari and Sleep 1991; Barker et al. 1994; Kelemen et al. 2003, 2014; Mehl et al. 2003; Clift et al. 2005; Behn and Kelemen 2006; Greene et al. 2006; Amato et al. 2007; Rioux et al. 2007; Hacker et al. 2008, 2011; DeBari and Greene 2011; Jagoutz and Kelemen 2015) and therefore represents a well-characterized locality to quantify the f_{O_2} of both the sub-arc mantle and primitive ultramafic cumulates at the base of the crust. Further, we compare our estimates of upper mantle and lower crustal f_{O_2} to redox-sensitive element ratios in Talkeetna volcanic rocks to determine whether these ratios are consistent with the f_{O_2} of their source region.

Regional geologic setting and samples

The accreted, Jurassic Talkeetna arc comprises the Peninsular terrane of south-central Alaska, bounded to the north by flood basalts and Paleozoic arc-related rocks of the Wrangellia terrane and to the south by the accretionary complexes of the Chugach terrane along the Border Ranges Fault (BRF, Fig. 1, Pavlis 1982, 1983; Plafker et al. 1989; Burns et al. 1991). The Talkeetna arc was active from ~ 200 to 170 Ma (Rioux et al. 2007, 2010) and accreted to North America in the Late Jurassic or Early Cretaceous (Plafker et al. 1989; Rioux et al. 2007, 2010). The arc is composed of a faulted, but complete section of sedimentary, volcaniclastic,

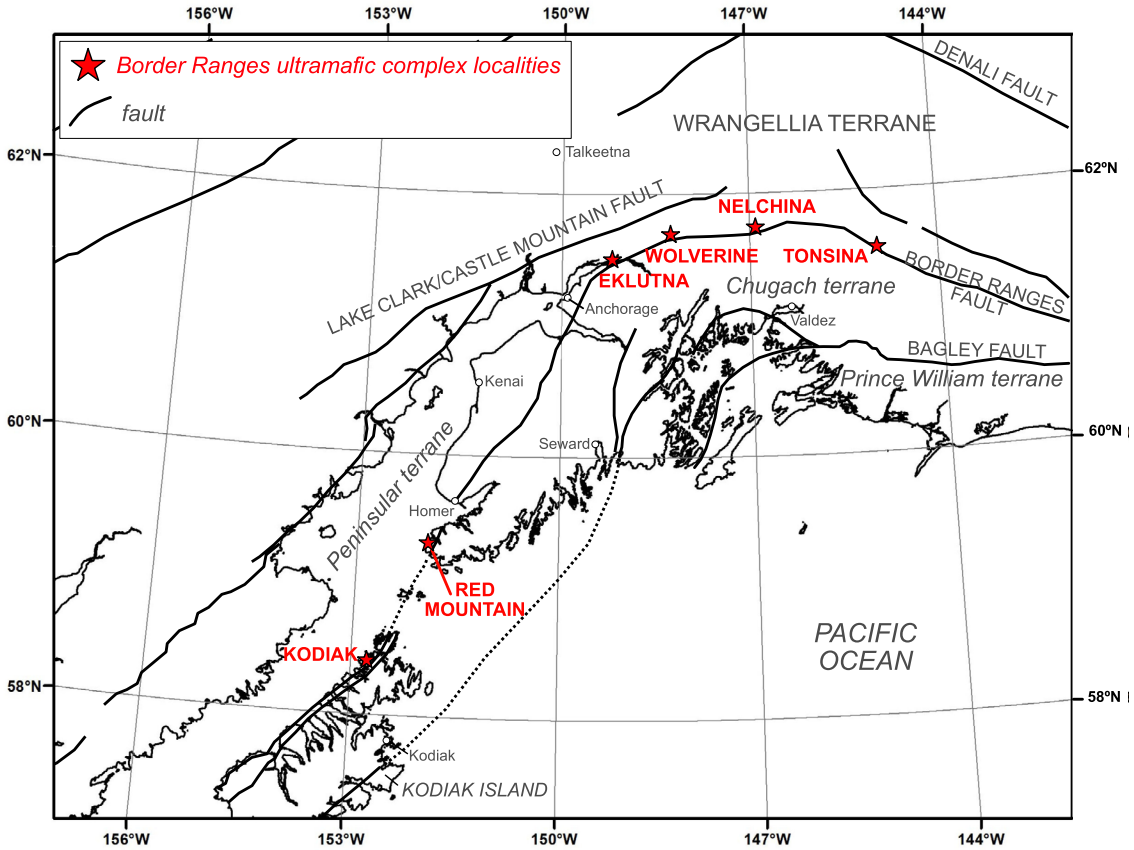

Fig. 1 Map of south central Alaska showing major geologic terrane boundaries and faults as well as the Border Ranges ultramafic complex localities. Samples studied here are from Red Mountain, Eklutna, and Tonsina. The map is projected in Lambert Conformal Conic in the geographic system GCS North American 1983. Faults are from Wilson et al. (2015) (USGS Scientific Investigations Map 3340)

hypabyssal, plutonic, and peridotitic mantle rocks from north to south (Burns 1985; Barker and Grantz 1986; DeBari and Coleman 1989; Plafker et al. 1989; Mehl et al. 2003; Clift et al. 2005; Greene et al. 2006). Evidence for pre-existing crust in the Talkeetna arc section is limited to inherited zircon in plutons near the suture with the Wrangellia terrane (Rioux et al. 2007, 2010) and in the western part of the arc on the Alaskan Peninsula (Amato et al. 2007). Further, Nd and Sr isotope ratios for plutonic and volcanic rocks overwhelmingly suggest limited contribution from pre-existing crust and formation in an oceanic setting (Clift et al. 2005; Greene et al. 2006; Rioux et al. 2007, 2010). Thermobarometry from the base of the crust indicates equilibration at ~1 GPa and ~1000 °C (Kelemen et al. 2003; Hacker et al. 2008), typical for a ~40 km thick intra-oceanic arc. Using thicknesses of the coeval volcanic section (Clift et al. 2005) and thermobarometry on igneous and metamorphic rocks at various depths within the arc, Hacker et al. (2008) and Jagoutz and Kelemen (2015) reconstructed a vertical cross section through the arc as comprising 5–7 km of volcanic rocks, 4–14 km of felsic plutonic rocks, 9–16 km of mafic plutonic rocks, and 4–10 km of a basal garnet gabbronorites, and a few hundred meters of primitive, ultramafic cumulates, overlying residual mantle peridotites.

In this study, we focus on exposures of primitive ultramafic and mafic rocks at the base of the Talkeetna arc and describe them in more detail here. Six ultramafic localities have been described along the BRF, including, from southwest to northeast, those on Kodiak Island (Beyer 1980), Red Mountain on the Kenai Peninsula (Toth 1981), Eklutna (Rose 1966), the Wolverine complex (Clark 1972; Kusky et al. 2007), the Nelchina complex (Burns 1985), and the Tonsina complex (Burns 1985; Debari and Coleman 1989) (Fig. 1). The southernmost exposures on Kodiak Island and at Red Mountain on the Kenai Peninsula are dominated by cumulate dunite (Beyer 1980). We studied three dunites (± clinopyroxene) and wehrlites from Red Mountain (Table 1). In the Chugach Mountains, the exposure of ultramafic rocks is in the Eklutna complex, which is characterized by > 600 m-thick cumulate sequences that extend

Table 1 Sample summary

Sample	Location	Lithology	Mineralogy									Petrography
			Olivine		Opx		Cpx		Spinel		Serp. (%[b])	
			%[b]	Grain size (mm)	%[b]	Grain size (mm)	%[b]	Grain size (mm)	%[b]	Grain size (mm)		
0803L01F	Bernard Mountain, Tonsina	Lherzolite	66.7	0.2–1	18.7	0.2–2	11.3	0.2–0.4	3.3	0.2–0.5	< 5	Large opx grains (0.8–2 mm) surrounded by recrystallized ol and cpx. Occasional spinel poikilitically enclosed in opx. Granoblastic
1709P02	Bernard Mountain, Tonsina	Dunite	96.4	0.1–0.2	–	–	–	–	3.6	0.05–0.3	10	Ol fractured and serpentinized along rims and fractures
1802L07	Bernard Mountain, Tonsina	Dunite (+cpx)	94.5	0.3–0.9	–	–	3.1	0.2–0.5	2.4	0.07–0.6	5	Ol fractured and serpentinized along rims and fractures. Sp is euhedral and evenly distributed among ol
1805L01	Bernard Mountain, Tonsina	Dunite (+cpx)	96.7	0.2–3.6	–	–	0.8	0.3–0.5	2.5	0.08–0.4	~3	Sp anhedral to subhedral. Granoblastic olivine
1710G01	Sheep Mountain, Tonsina	Harzburgite	56.4	0.3–3	30.9	1.7–3.1	3.6	1.1–2.8	9.1	0.05–0.3	~8	Ol generally > 1 mm in diameter. Some serpentinization of olivine and opx. Anhedral to subhedral spinel grains. Cpx very sparse. Granoblastic
1710P03	Sheep Mountain, Tonsina	Lherzolite	53.3	0.2–0.8	22.9	0.5–2	19.0	0.2–1.5	4.8	0.1–0.4	< 2	Granoblastic. Sp occasionally poikilitically enclosed in opx
1710P11	Sheep Mountain, Tonsina	Olivine websterite	35.9	0.1–1.1	53.0	0.8–2.2	7.7	0.1–0.5	3.4	0.1–0.6	~3	Anhedral granoblastic grains. Serpentinite minimal
1710P12	Sheep Mountain, Tonsina	Wehrlite	74.8	0.1–2.2	–	–	21.6	0.3–1.9	3.6	0.1–0.4	–	Anhedral granoblastic grains. Serpentinite minimal

Table 1 (continued)

Sample	Location	Lithology	Mineralogy									Petrography
			Olivine		Opx		Cpx		Spinel		Serp. (%[b])	
			%[b]	Grain size (mm)	%[b]	Grain size (mm)	%[b]	Grain size (mm)	%[b]	Grain size (mm)		
2808L04	Eklutna	Spinel-rich dunite (+cpx)	58.4	0.6–3.4	–	–	7.1	0.5–1.4	34.4	0.1–2.2	~28	Anhedral granoblastic grains. Heavy serpentinization. Sp is subhedral to rounded. Cpx is interstitial
2808L06	Eklutna	Dunite	94.3	1.2–3.3	–	–	–	–	5.7	0.1–0.8	~15	Sp poikilitically enclosed within ol. Sp subhedral to rounded. Ol fractured and filled with serpentinite
2809L02	Eklutna	Dunite (+cpx)	92.7	0.7–3.3	–	–	5.6	0.4–0.6	1.6	0.1–0.4	~6	Serpentinite veining. Sp poikilitically enclosed in ol or along grain boundaries. Sp subhedral to rounded
2809L03[a]	Eklutna	Wehrlite	61.1	0.5–4.4	–	–	12.4	0.3–1.0	26.5	0.1–1.4	~5	Accumulation of sp in corner of thin section. Cpx is interstitial and only found associated with spinel accumulation. The rest of thin section is dunite. Sp is subhedral to rounded. Point counting is done for sp accumulation and dunite. Sp generally larger in accumulation
		Dunite	97.8	–	–	–	–	–	2.2	–		
2813L01	Red Mountain	Wehrlite	88.7	0.03–0.2	–	–	9.6	0.05–0.1	1.7	0.2–0.6	~2	Mylonitic texture. Granoblastic groundmass of ol and cpx with larger grains of ol (0.5–2 mm) and sp (0.2–0.6 mm). Grain size given in table is for ground mass

Table 1 (continued)

Sample	Location	Lithology	Mineralogy									Petrography
			Olivine		Opx		Cpx		Spinel		Serp. (%[b])	
			%[b]	Grain size (mm)	%[b]	Grain size (mm)	%[b]	Grain size (mm)	%[b]	Grain size (mm)		
2814L07	Red Mountain	Dunite (+cpx)	92.9	0.03–0.3	–	–	< 1	< 0.05	7.1	0.1–0.8	~ 3	Mylonitic texture. Groundmass of ol and minor cpx with larger grains of olivine (0.7–1.4 mm) and sp (0.1–0.8 mm). Grain size given in table is for ground mass. Sp grains elongated and aligned along foliation. Ol grains highly fractured. Small sp accumulation in lower corner of thin section
2814L09	Red Mountain	Dunite	83.0	< 0.1–1.0	–	–	–	–	17.0	0.05–0.8	< 2%	Lower 1/3 of thin section has dense accumulation of sp. Point counts are for dunite in other 2/3s of thin section. Dunite is fine-grained granoblastic. Larger ol grains are elongate in direction perpendicular to layering of sp. Spinel grains sub- to euhedral and brownish

cpx clinopyroxene, *ol* olivine, *opx* orthopyroxene, *sp* spinel

[a]See Supplementary Information for description of different lithologies in this sample

[b]Modal %

~ 11 to 12 km along the BRF and transition from chromite-bearing dunite in the south to websterite and gabbro in the northern, higher level exposures (Rose 1966). We studied four samples (3 dunites and 1 wehrlite) from Eklutna. The easternmost exposure of ultramafic rocks is the Tonsina complex, comprising four peaks: Bernard, Sheep, Dust, and Scarp Mountains. The Bernard Mountain section of the Tonsina is the best exposed and most extensively studied (e.g., Debari and Coleman 1989; Mehl et al. 2003). Bernard Mountain exposes a complete section of residual peridotite to the south in contact with the BRF to the garnet gabbros in the northernmost exposure. ~ 2500 m of residual spinel harzburgite with interlayered dunite are found at the base which is successively overlain by a ~ 100-m-thick transition zone of chromite-bearing dunite, 50–200 m of websterite, orthopyroxenite, clinopyroxenite, and olivine clinopyroxenite, and ~ 250 m of garnet-bearing gabbro, norite, and gabbronorite (see Fig. 3 of DeBari and Coleman 1989 or Fig. 2 of Mehl et al. 2003). The crust–mantle transition in the Tonsina region is defined by contact between the lherzolites/harzburgites and the dunites/clinopyroxene-dominated lithologies. We studied one lherzolite, one harzburgite, one olivine websterite, and one wehrlite from Sheep Mountain and one lherzolite and three dunites (± clinopyroxene) from Bernard Mountain. The lherzolites and harzburgites are thought to represent residual mantle tectonite based on the presence of plastically deformed spinel and orthopyroxene and the lack of significant clinopyroxene (generally, < 10%) (Mehl et al. 2003).

Petrography

Mineral modal percentages (point counting), grain sizes, and sample petrographic descriptions are included in Table 1.

Tonsina lherzolites, olivine websterite, and harzburgite

These lithologies are composed of ~ 36 to 67% olivine, 19–53% orthopyroxene, 4–19% clinopyroxene, and 3–9% spinel. All samples are recrystallized as demonstrated by granoblastic textures (Fig. 2a) and low cation exchange temperatures (Fig. 4). Grain size of silicates is variable among samples from < 100 to ~ 3 mm in diameter. Spinels are tens to hundreds of micrometers in diameter and occur in external contact with other silicates, as well as poikilitically enclosed within orthopyroxene. Serpentine is present along the grain boundaries and internal mineral fractures in all samples, but relatively in minor amounts (< 10% of rock volume) (Fig. 2a).

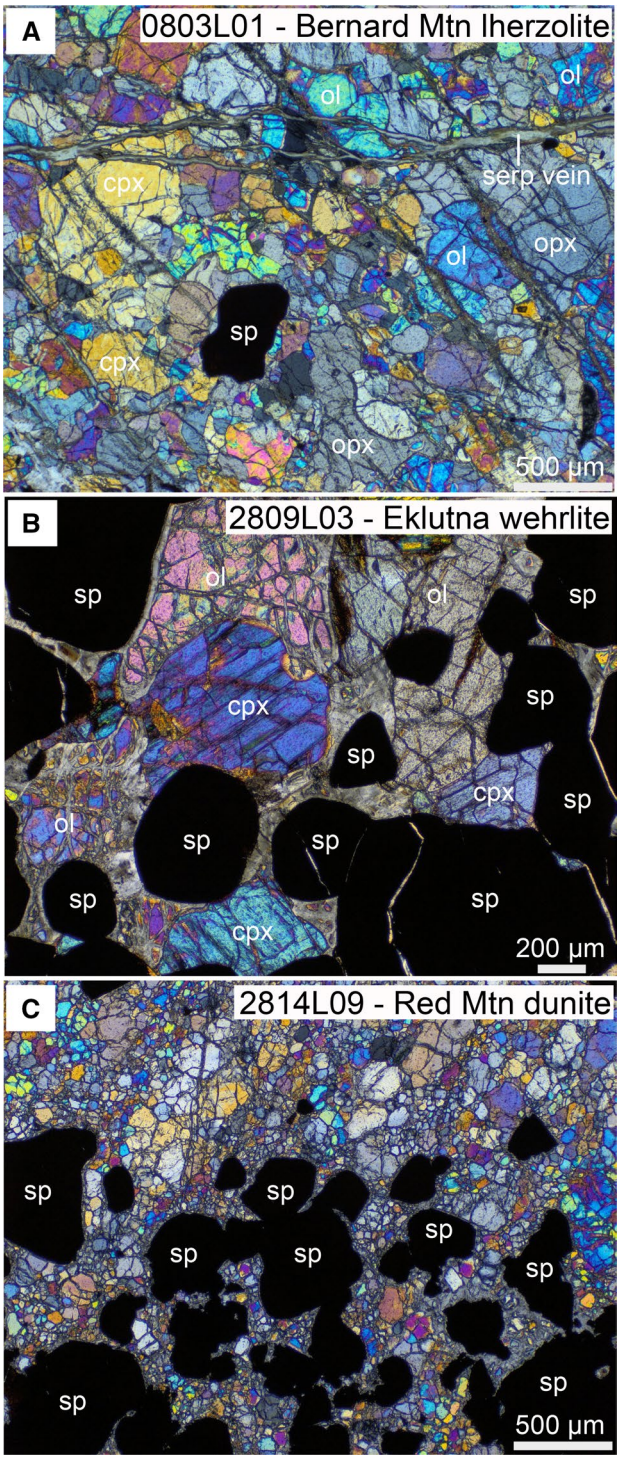

Fig. 2 Photomicrographs of representative sample thin sections in cross-polarized light. **a** Bernard Mountain (Tonsina) lherzolite (0803L01). Note serpentinite veins and recrystallized texture. **b** Eklutna spinel-rich wehrlite (2809L03) with cumulus olivine, clinopyroxene, and spinel. **c** Red Mountain dunite (2814L09) with coarse cumulus spinel in a fine-grained re-crystallized olivine matrix. Images from **b** and **c** have higher modal proportions of spinel than those reported in Table 1 due to the relatively small area represented in the image (as compared to the entire thin section) and the fact that the photos highlight particularly spinel-rich sections

Tonsina wehrlite and dunites (± clinopyroxene)

The wehrlite from Sheep Mountain (1710P12) contains olivine (74.8%), clinopyroxene (21.6%), and spinel (3.6%). Three dunites from Bernard Mountain contain 94.5–96.7% olivine and 2.5–3.6% spinel. Two of the dunites contain minor amounts of clinopyroxene (0.8–3.1%). All samples are granoblastic. Grain size is variable among samples from fine-grained 50–300 μm (e.g, 1709P02) to olivine grains up to 3.6 mm in diameter (e.g, 1805L01). Spinels in samples are 50–600 μm in diameter. Olivine in two of the samples is fractured and serpentinized along the rims and fracture planes. Serpentine comprises < 10% of samples.

Eklutna dunites and wehrlites

The four samples from Eklutna include a spinel-rich dunite (2808L04), a dunite (2808L06), a clinopyroxene-bearing dunite (2809L02), and a spinel-rich wehrlite (2809L03; Fig. 2b). All samples from Eklutna display orthocumulate or cumulate textures dominated by olivine and/or spinel. The spinel-rich dunite contains 58.4% olivine, 7.1% clinopyroxene, and 34.4% spinel. The other dunites contain 92.7–94.3% olivine, 0–5.6% clinopyroxene, and 1.6–5.7% spinel. One corner of the thin section studied of 2809L03 contains a wehrlitic modal assemblage: 61.1% olivine, 12.4% clinopyroxene, and 26.5% spinel (Fig. 2b). The remainder of the thin section is a clinopyroxene-free dunite. Spinels from all samples are subhedral to rounded and sometimes found poikilitically enclosed within olivine. Clinopyroxene is interstitial. Serpentinization is variable (5–28%), being most extensive in samples 2808L04 (~ 28%) and 2808L06 (~ 15%). All samples are coarse grained with olivines and spinels having diameters of 3–4 mm and 1–2 mm, respectively.

Red Mountain dunites (± clinopyroxene)

The three samples from Red Mountain are dunites (83.0–92.9% olivine) with spinel (1.7–17.0%). Two of the samples also contain minor clinopyroxene (< 1 to 9.6%). All samples are deformed with mylonitic textures characterized by a fine-grained (30–300 μm) groundmass of olivine ± clinopyroxene and larger (1–2 mm) olivine crystals and spinel grains (≤ 800 μm) aligned along sample foliation. Olivines in groundmass are granoblastic. Sample 2814L09 contains a dense accumulation of chromite grains with orthocumulate textures (Fig. 2c). Serpentine comprises < 3% of these samples.

Methods

Electron microprobe analyses

We analyzed major, minor, and trace element compositions of olivine, orthopyroxene, clinopyroxene, and spinel at the California Institute of Technology using a JEOL JXA-8200 electron microprobe. SiO_2, TiO_2, Al_2O_3, Cr_2O_3, V_2O_3, FeO, MnO, MgO, CaO, NiO, ZnO, Na_2O, and K_2O were analyzed using an accelerating voltage of 15 kV, a 25 nA beam current, and a 1 μm spot size. A full description of analytical conditions can be found in Table S1, including primary standards, count times, and detector crystals. When possible, we chose primary standards compositionally similar to our unknowns. X-ray intensities were converted to oxide concentrations using a modified ZAF procedure (CITIZAF, Armstrong 1995). The detection limits for the analytical conditions used were < 0.01 wt% for SiO_2, Al_2O_3, MgO, CaO, K_2O, Na_2O, V_2O_5; 0.01 wt% for TiO_2, FeO, Na_2O, Cr_2O_3, MnO, 0.02 wt% for NiO, and 0.03 wt% for ZnO. The range of observed 1σ relative errors (percent of absolute value) for different mineral analyses calculated from counting statistics is given in Table S1. Analyses were focused on the cores of minerals and ~ 5 to 20 different grain cores from each sample were analyzed; however, rims were also analyzed to check for intra-grain heterogeneity. In addition, in three samples core to rim traverses of spinels with analytical points spaced every 7–12 μm were done. Unknown spinel analyses were bracketed with 11 spinel standards (provided by B. Wood) with Fe^{3+}/Fe^{T} ratios previously determined by Mössbauer spectroscopy (Wood and Virgo 1989; Bryndzia and Wood 1990). Each standard spinel was measured three times at the beginning and end of each analytical session. These analyses were then used to correct the Fe^{3+}/Fe^{T} ratios in our unknown samples (see "Calculation of Fe^{3+}/Fe^{T} in spinel" and Table S2).

We conducted a separate analytical session focused on high precision analysis of Ca in olivine. A synthetic anorthite standard (P-80) was used as a primary standard. Ca was measured on a PETL crystal using a 10 μm spot size, an accelerating voltage of 10 kV, and a 200 nA beam current on spots previously analyzed using the conditions described in the previous paragraph. Ca was measured for 600 s on peak and 300 s on the background on either side of the peak. Previously analyzed Fe, Mg, and Si concentrations were used for matrix corrections. Using this analytical protocol, the limit of detection was 10 ppm and relative errors (1σ) on CaO concentrations were ± 1.2 to 6.5%. These analytical protocols are similar to those previously reported (e.g, Coogan et al. 2002; VanTongeren et al. 2008). As most of the samples analyzed were

clinopyroxene bearing, we took precautions to only analyze olivine cores to avoid secondary X-ray fluorescence (e.g, Dalton and Lane 1996). Although we did not have an external Ca-bearing olivine standard to assess accuracy, our measured Ca contents are similar to that previously reported for Talkeetna lower crustal rocks (unpublished data, K. Hanghøj; see Fig. 8 of VanTongeren et al. 2008).

Calculation of Fe^{3+}/Fe^{T} in spinel

Implementation of the oxybarometry based on exchange of Fe between olivine and spinel requires accurate and precise quantification of spinel Fe^{3+}/Fe^{T} ratios (Wood and Virgo 1989; Davis et al. 2017). Spinel Fe^{3+}/Fe^{T} ratios can be determined by EMPA measurement by assuming an ideal stoichiometry of the spinel phase (i.e, $A^{2+}B_2^{3+}O_4$) and by assigning cations of Fe as ferric in proportion to charge imbalances. This method can lead to large uncertainties on calculated Fe^{3+}/Fe^{T} ratios because analytical uncertainties for each measured oxide are propagated through the calculation and any unmeasured elements present in the spinel will lead to erroneously high Fe^{3+}. To increase the accuracy of EMPA measurements, Wood and Virgo (1989) presented a correction procedure (hereafter referred to as the "W&V89 correction") involving the analysis of a spinel standard set previously characterized for Fe^{3+}/Fe^{T} ratios by bulk Mössbauer spectroscopy during EMPA analysis. They reported a linear correlation between the difference in Fe^{3+}/Fe^{T} ratio measured by Mössbauer and calculated by EPMA analysis and the Cr# (molar Cr/[Cr + Al]) in spinels, which can then be used to correct unknown values: $Fe^{3+}/Fe^{T}_{\text{Mössbauer}} - Fe^{3+}/Fe^{T}_{\text{EMPA}} = A*Cr\# + B$. Although this correction has not been uniformly adopted by subsequent studies due to disagreement over its effectiveness or necessity, Davis et al. (2017) systematically assessed the W&V89 correction through replicate EMPA analyses of spinels previously characterized by Mössbauer spectroscopy and demonstrated that the correction substantially improved both accuracy and precision of spinel Fe^{3+}/Fe^{T} ratios determined by EMPA. As such, we adopt the W&V89 correction in our spinel analyses.

We calculated the Fe^{3+}/Fe^{T} ratios of the standard spinels by initially treating all Fe as Fe^{2+}, normalizing the spinel cation proportions to three cations total, and then adjusted the Fe^{3+}/Fe^{T} ratios to balance the charge deficiencies. We then used the averages of replicate standard analyses to generate the W&V89 correction for each daily analytical session (see Table S2 for standard spinel correction dataset). This correction was then used to calculate the Fe^{3+}/Fe^{T} ratios of unknown spinels measured during that session. This correction resulted in a shift in the average Fe^{3+}/Fe^{T} ratios in spinels of samples by −0.039 to +0.054 (average shift of -0.006 ± 0.059, 2σ).

Results

Mineral chemistry

The compositions of mineral cores are summarized in Table 2 (and given in full in Tables S3–S6). Mineral compositions are consistent with those previously published for the Tonsina complex (DeBari and Coleman 1989; Fig. 3). Sample average Mg# (molar Mg/[Mg + Fe] × 100) of olivine cores vary between 81.9 and 91.5 (except for two spinel-rich samples with olivine Mg# of 93.0 (2808L04) and 95.3 (2814L09), Fig. 3a). Intrasample olivine Mg# variability (reported as 2σ on sample averages) is between 0.20 and 0.82 (except for sample 1710G01 with $2\sigma = 1.37$). Average NiO contents in olivine range from 0.09 to 0.44 wt% and are positively correlated with olivine Mg# (Fig. 3a). Average Ca concentrations in olivine vary between 61 and 389 ppm and do not vary systematically with lithology or olivine major/minor element composition. The observed intrasample variance in Ca concentrations is between 20 and 107 ppm (2σ on sample averages).

Clinopyroxene Mg# sample averages vary between 87.8 and 95.6. Average clinopyroxene Al_2O_3 contents range from 0.42 to 2.95 wt% and are negatively correlated with Mg# ($R^2 = 0.61$). Average clinopyroxene Cr_2O_3 contents vary between 0.18 and 0.75 wt%. Orthopyroxene was analyzed in the four lherzolite and harzburgite samples (see Table 1). Orthopyroxene Mg# sample averages range from 83.2 to 91.0. Average orthopyroxene Al_2O_3 concentrations vary between 1.28 and 2.65, CaO concentrations between 0.35 and 0.49 wt%, and Cr_2O_3 concentrations between 0.21 and 0.36 wt%. Olivine, clinopyroxene, and orthopyroxene Mg# from the same samples are all linearly correlated (Fig. 3b) with olivine–clinopyroxene and olivine–orthopyroxene pairs preserving an average $K^{Fe^T/Mg}_{\text{ol - min}}$ (molar $\frac{(Fe^T/Mg)_{ol}}{(Fe^T/Mg)_{cpx\ or\ opx}}$) of 1.85 ± 0.44 and 1.06 ± 0.08 (2σ).

Sample average spinel Cr# [molar 100*Cr/(Cr + Al)] varies between 29.5 and 79.5, with a lherzolite and a harzburgite from Tonsina preserving the lowest spinel Cr# of 29.5 and 32.0. The other 13 samples have average spinel Cr# between 46.8 and 79.5 (Fig. 3c–e). Average spinel Cr# is inversely correlated with average clinopyroxene Al_2O_3 contents (Fig. 3d). Spinels have Mg# between 29.3 and 60.1 (Fig. 3c). Sample average Fe^{3+}/Fe^{T} ratios in spinel vary from 0.160 to 0.330, consistent with the range observed in spinels from arc peridotite xenoliths (Fig. 3e). No systematic variation is observed with Mg# of coexisting silicates and spinel Cr#.

Spinels in 11 samples lack core-to-rim zonation. However, in three samples spinel rims exhibited both lower (samples 1710P12) and higher (1709P02 and 1805L01) Fe^{3+}/Fe^{T} ratios. In the two samples with elevated Fe^{3+}/Fe^{T} ratios on

Table 2 Summary of sample average mineral chemistry (core analyses)

Sample	Olivine						Orthopyroxene				Clinopyroxene						Spinel[a]					
	Mg#	2σ	NiO	2σ	Ca (ppm)	2σ	Mg#	2σ	Al_2O_3 (wt%)	2σ	Mg#	2σ	Al_2O_3 (wt%)	2σ	Cr_2O_3 (wt%)	2σ	Cr#	2σ	Mg#	2σ	Fe^{3+}/Fe^{T}	2σ
0803L01F	90.8	0.3	0.38	0.05	79	22	91.0	0.6	1.28	0.49	94.5	0.9	1.25	0.34	0.46	0.20	58.5	3.2	55.2	3.9	0.19	0.05
1709P02	91.3	0.2	0.23	0.02	388	101	–	–	–	–	–	–	–	–	–	–	78.4	1.9	39.0	4.7	0.22	0.03
1802L07	91.5	0.2	0.23	0.05	338	106	–	–	–	–	95.4	0.5	0.55	0.12	0.38	0.13	79.5	0.9	55.8	3.5	0.24	0.03
1805L01	89.2	0.5	0.22	0.04	190	67	–	–	–	–	94.2	0.8	0.69	0.23	0.37	0.23	73.8	3.0	57.3	1.9	0.27	0.05
1710G01	81.9	1.4	0.09	0.04	159	53	83.2	0.3	2.37	0.78	87.8	0.4	2.82	0.72	0.44	0.14	32.0	4.9	59.7	4.1	0.29	0.03
1710P03	87.6	0.3	0.20	0.03	156	94	87.9	0.3	2.80	0.39	91.1	1.0	2.95	1.02	0.65	0.30	29.5	2.7	56.9	2.8	0.16	0.06
1710P11	84.9	0.7	0.16	0.04	83	20	85.9	0.3	1.33	0.61	91.5	0.6	0.98	0.18	0.35	0.13	61.4	4.0	29.1	4.4	0.30	0.02
1710P12	83.9	0.8	0.12	0.03	180	87	–	–	–	–	90.8	1.4	1.57	0.57	0.38	0.14	46.8	5.0	31.8	4.1	0.32	0.03
2808L04	93.0	0.5	0.40	0.03	61	25	–	–	–	–	95.4	1.2	0.81	0.45	0.50	0.18	70.4	1.1	49.7	4.3	0.28	0.05
2808L06	88.5	0.4	0.26	0.04	182	63	–	–	–	–	–	–	–	–	–	–	74.2	1.5	31.0	4.4	0.33	0.02
2809L02	87.6	0.3	0.20	0.03	100	59	–	–	–	–	92.8	1.2	1.36	0.69	0.38	0.30	50.2	1.9	43.3	2.0	0.20	0.03
2809L03	91.1	0.4	0.30	0.05	101	66	–	–	–	–	95.6	0.4	1.54	0.31	0.75	0.35	51.7	0.9	54.2	3.1	0.21	0.05
2813L01	91.4	0.5	0.26	0.04	108	53	–	–	–	–	95.6	0.8	0.42	0.30	0.19	0.17	63.8	2.6	48.9	5.6	0.26	0.06
2814L07	89.9	0.5	0.25	0.04	163	43	–	–	–	–	95.0	1.0	0.42	0.41	0.19	0.15	67.6	2.5	40.6	3.7	0.33	0.03
2814L09	95.3	0.6	0.44	0.03	130	79	–	–	–	–	–	–	–	–	–	–	78.4	1.1	58.2	2.8	0.25	0.04

Reported 2σ variability on all analyses represents intrasample variation

[a]Reported Fe^{3+}/Fe^{T} values are W&V89 corrected values except for 1709P02, for which analyses were not bracketed with spinel standards and therefore not corrected

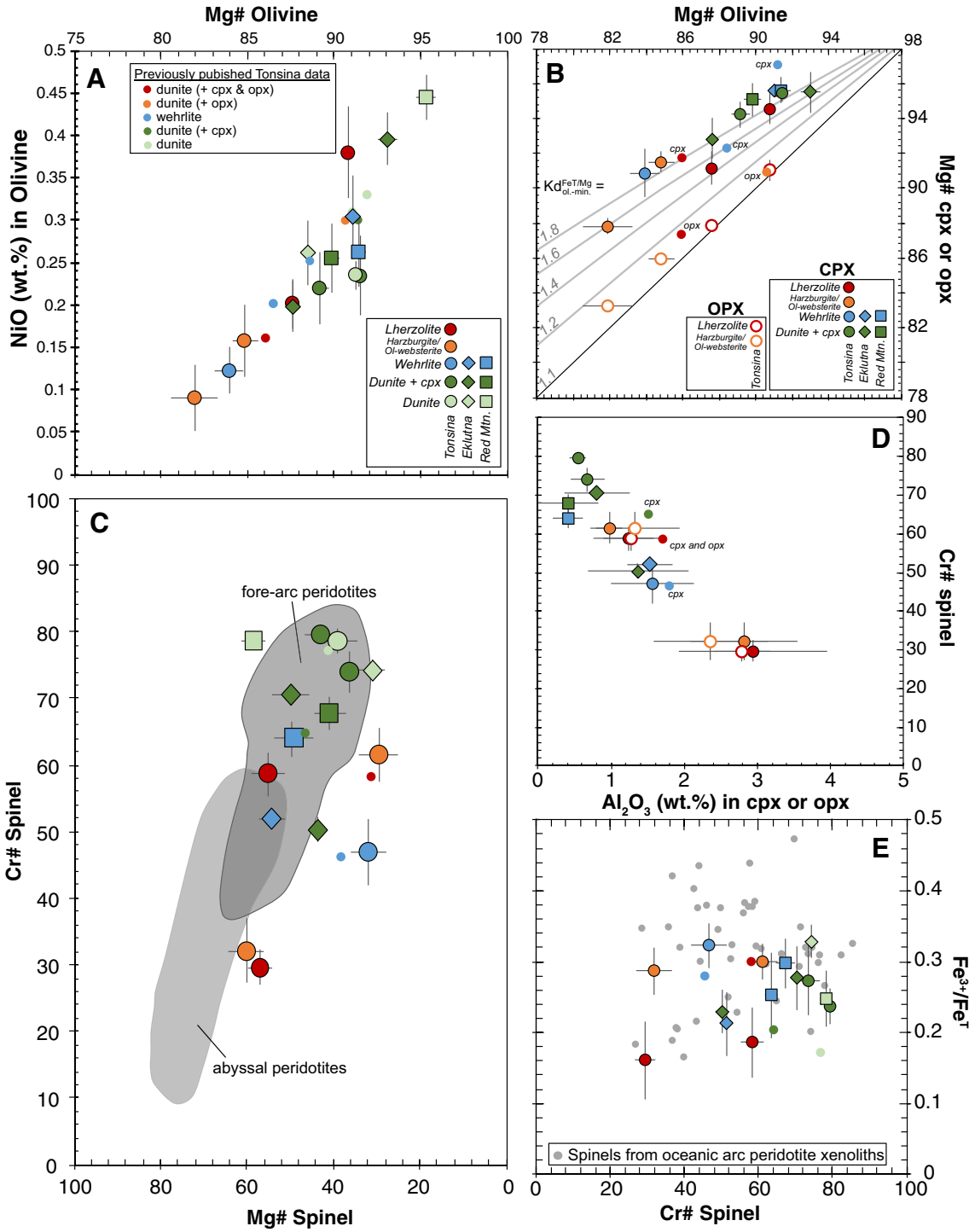

Fig. 3 Summary of mineral chemistry. Individual data points represent sample averages and error bars 2σ on the sample averages. **a** NiO (wt.%) in olivine versus Mg# of olivine. **b** Mg# in clinopyroxene or orthopyroxene versus olivine. **c** Cr# (Cr/[Cr+Al]) versus Mg# (Mg/[Mg + Fe^{2+}]) in spinel. Abyssal peridotite field after Dick and Bullen (1984) and Warren (2016) and fore-arc peridotite field is after Arai and Ishimaru (2008) (and references therein). **d** Cr# in spinel versus Al_2O_3 (wt.%) in clinopyroxene and orthopyroxene. **e** Fe^{3+}/Fe^{T} versus Cr# in spinel. Previously published data from Tonsina is from DeBari and Coleman (1989). Data for spinels from oceanic arc xenoliths is from Solomon and Vanuatu (Parkinson and Arculus 1999; Barsdell and Smith 1989) and the Lesser Antilles (Parkinson et al. 2003)

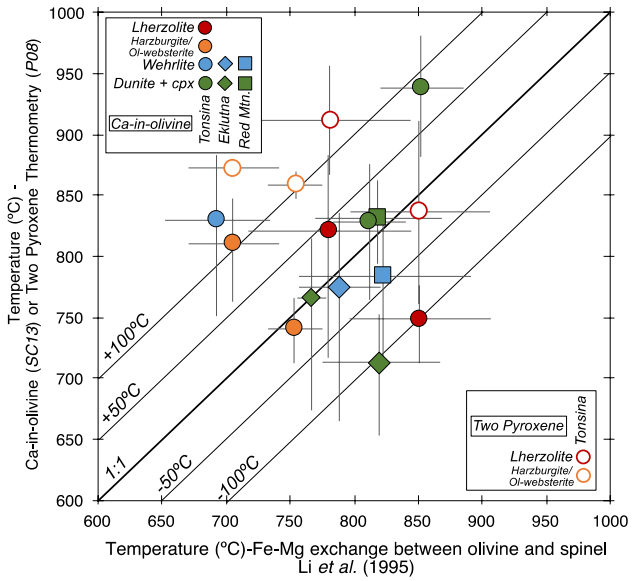

Fig. 4 Comparison of calculated equilibration temperatures using Fe–Mg exchange thermometry between olivine and spinel (Li et al. 1995), Ca-in-olivine thermometry (Shejwalkar and Coogan 2013), and two pyroxene thermometry (Putirka 2008). Ca-in-olivine temperatures were calculated using equation 13 of Shejwalkar and Coogan (2013) which accounts for the effect of pressure on Ca exchange between olivine and pyroxenes. Two pyroxene thermometry was calculated using Equation 36 of Putirka 2008. No data is shown for the clinopyroxene-lacking dunite samples because Ca-in-olivine temperatures could not be calculated due to lack of pyroxenes. Using the thermometer of Li et al. (1995) temperature estimates for the dunites are 780 ºC, 1089 ºC, and 817 ºC (see Table 3)

the rims, core to rim traverses were undertaken demonstrating that the rims with higher Fe^{3+}/Fe^{T} ratios (by up to 0.25) extended 40–60 µm into the spinel crystals (Fig. S1).

Discussion

Pressure and temperature

We implemented a pressure of 1 GPa for all calculations following previous estimates for the base of the Talkeetna arc crust (Hacker et al. 2008). For temperature, three different thermometers were implemented. For all samples, the olivine–spinel Fe–Mg exchange thermometer of Li et al. (1995) was applied using sample average olivine and spinel core compositions. Calculated temperatures were between 690 and 855 °C with one outlier (sample 2814L09) that preserved a temperature of 1100 °C (Fig. 4). For the four orthopyroxene- and clinopyroxene-bearing samples (i.e., lherzolites and clinopyroxene-poor harzburgites), two pyroxene thermometry (using Eq. 36 of Putirka 2008) was applied using average pyroxene core compositions, yielding temperatures of 830–915 °C. Last, for clinopyroxene- and olivine-bearing samples (i.e., lherzolites and wehrlites, $n = 11$), the temperatures were also calculated using the experimentally derived thermometer based on the equilibrium exchange of Ca between coexisting olivine and pyroxenes of Shejwalkar and Coogan (2013). The thermometer of Shejwalkar and Coogan (2013) (their equation 111) is for low pressures (0.1 MPa); however, they also provide a synthesis of data obtained from experiments conducted from 0.1 MPa to 6 GPa and a preliminary thermobarometer (their equation 113) similar to that of previous studies (e.g, Köhler and Brey 1990; Adams and Bishop 1986). We applied both the 0.1 MPa thermometer and the thermobarometer calculated at 1.0 GPa. Calculated temperatures range from 765 to 948 and 712 to 937 °C, respectively, with the pressure-corrected temperature estimate being 35 ± 23 °C lower on average than the non-pressure-corrected estimates.

Temperature estimates using the three different thermometers within a single sample broadly preserve the same values (between 700 and 950 °C and mostly within ± 100 °C of each other; Fig. 4). They are lower than those expected for olivine-dominated crystallization assemblages in hydrous arc magmas (> 1050 °C; Nandedkar et al. 2014). The lower temperatures yielded by the thermometers indicates subsolidus cation exchange between minerals. The difference in temperatures and lack of correlation recorded by the different thermometers (Table 2, Fig. 4) likely reflect both the large uncertainties (10–100 °C, based on 2σ intrasample variation) associated with these calculations and different effective closure temperatures of the systems to subsolidus exchange (Dohmen et al. 2017).

Calculation of oxygen fugacity

A difficulty sometimes encountered when calculating f_{O_2} is the lack of an appropriate phase assemblage required for well-calibrated oxybarometers based on exchange of Fe between coexisting phases. The samples from the base of the Talkeetna arc are no exception. The four mantle samples have olivine, orthopyroxene, and spinel present, and therefore f_{O_2} can be thermodynamically assessed using the well-established olivine–orthopyroxene–spinel oxybarometer (e.g, Mattioli and Wood 1988; Ballhaus et al. 1991; Davis et al. 2017). However, the other 11 samples, while all containing olivine and spinel, lack orthopyroxene, which is required when implementing olivine–orthopyroxene–spinel oxybarometery to quantify the activity of SiO_2 (a_{SiO_2}). Clinopyroxene is present in 8 of the 11 samples. The remaining three samples are dunites with a phase assemblage of olivine and spinel. Due to the different phase assemblages present, we calculated f_{O_2} using several different methods, all based on the exchange of Fe between olivine and spinel, but using different equilibria to calculate a_{SiO_2}.

Table 3 Results of temperature, oxygen fugacity, and silica activity calculations

Sample	Temperature estimates (°C)							Silica activity estimates [$\log(a_{SiO_2})$]						Oxygen fugacity estimates (ΔFMQ)						
	Ol–Sp		Ca-in-olivine			Two Pyx.		Method A (based on Fo–CEn equilibria)			Method B (based on Di–Mo equilibria[d])			Method 1		Method 2		Method 3 (max a_{SiO_2} method A)	Method 4 (min. a_{SiO_2} method B)	
	L95		SC12			P08								B91		D17				
	Avg.	2σ[a]	Eq. (11)	Eq. (13)	2σ[b]	Avg.	2σ	Avg.	2σ[c]	ΔEn–Fo	Avg.	2σ[d]	ΔEn–Fo	Avg.	2σ[a]	Avg.	2σ[a]	Avg.	Avg.	2σ[a]
0803L01F	851	54	793	748	+23/−29	836	75	−0.99	+0.20/−0.50	−0.36	−0.61	+0.14/−0.11	+0.10	0.59	0.27	0.83	0.21	0.35	0.81	0.15
1709P02	817	8	965		+29/−36	–	–	–	–		–	–	–	1.38	0.04	–	–	–	–	–
1802L07	853	33	948	937	+34/−44	–	–	−1.69	+0.85	−1.06	−0.48	+0.16/−0.11	+0.10	1.50	0.15	–	–	0.13	0.71	0.19
1805L01	812	28	859	829	+37/−53	–	–	−1.16	+0.25/−0.38	−0.50	−0.50	+0.23/−0.15	+0.14	1.59	0.34	–	–	0.20	0.92	0.29
1710G01	706	35	838	811	+29/−39	871	6	−0.87	+0.13/−0.15	−0.13	−0.54	+0.18/−0.12	+0.11	1.71	0.21	1.25	0.19	0.86	1.22	0.16
1710P03	782	64	851	821	+50/−86	911	45	−0.80	+0.16/−0.35	−0.12	−0.57	+0.40/−0.20	+0.08	0.25	0.45	0.82	0.38	0.44	0.42	0.36
1710P11	754	21	783	741	+20/−24	858	11	−0.88	+0.11/−0.15	−0.18	−0.58	+0.12/−0.09	+0.14	1.72	0.07	1.25	0.19	1.05	1.38	0.21
1710P12	693	41	855	830	+42/−64	–	–	−0.92	+0.16/−0.33	−0.17	−0.52	+0.29/−0.17	+0.12	2.13	0.24	–	–	1.18	2.04	0.22
2808L04	821	46	765	712	+34/−51	–	–	−0.93	+0.2/−0.72	−0.28	−0.65	+0.27/−0.17	+0.09	2.02	0.16	–	–	2.25	2.25	0.12
2808L06	780	71	869		+32/−43	–	–	–	–	–	–	–	–	2.08	0.18	–	–	–	–	–
2809L02	767	11	806	765	+41/−77	–	–	−0.80	+0.19/−0.63	−0.11	−0.58	+0.38/−0.18	+0.11	0.93	0.12	–	–	1.28	1.92	0.04
2809L03	789	32	817	775	+50/−93	–	–	−1.16	+0.19/−0.79	−0.49	−0.58	+0.46/−0.22	+0.10	1.19	0.17	–	–	0.48	1.02	0.18
2813L01	824	67	824	784	+41/−63	–	–	−1.10	+0.31/−1.21	−0.45	−0.57	+0.30/−0.18	+0.10	1.63	0.18	–	–	0.88	1.10	0.15
2814L07	819	49	862	831	+25/−31	–	–	−1.41	+0.37	−0.76	−0.53	+0.13/−0.10	+0.11	2.06	0.10	–	–	0.30	1.51	0.16
2814L09	1089	43	855		+51/−88	–	–	–	–	–	–	–	–	0.81	0.18	–	–	–	–	–

[a]First, for each spinel grain analyzed, analyses of the cores (generally 2–4) were averaged. Then, these average spinel grain analyses (generally 8–12 per sample) were combined with the sample average olivine composition to obtain a temperature and olivine compositions plus silica activity estimates to obtain f_{O_2}. The error reported represents the error on the average of these temperature and f_{O_2} estimates

[b]Calculated using mole fractions of forsterite and monticellite in olivine based on 2σ variations Ca in olivine

[c]Maximum values calculated using highest MgO and lowest CaO contents of clinopyroxene and minimum values calculated (when possible) using lowest MgO and highest CaO contents of clinopyroxene (2σ variations on sample averages). These compositions were used to calculate the activity of clinoenstatite in clinopyroxene

[d]Calculated at Ca-in-olivine temperature (Shejwalkar and Coogan 2013; their Equation 13). Errors calculated using 2σ variations Ca contents in olivine

In olivine- and spinel-bearing rocks, the exchange of Fe between olivine and spinel may be used to quantify f_{O_2} using the heterogeneous equilibrium:

$$\begin{aligned} &3Fe_2SiO_4 + O_2 = 2Fe_3O_4 + 3SiO_2 \\ &3\,\text{fayalite} + O_2 = 2\,\text{magnetite} + 3SiO_2. \end{aligned} \quad (1)$$

The equilibrium constant for Eq. (1), denoted K_1, relates the ratio of the product to reactant activities:

$$K_1(T,P) = \frac{(a^{sp}_{mgt}[T,P,X])^2 * (a_{SiO_2}[T,P,X])^3}{(a^{ol}_{fa}[T,P,X])^3 * f_{O_2}}, \quad (2)$$

where T is the temperature, P is the pressure, X is the mole fraction, $a^{sp}_{Fe_3O_4}$ is the activity of magnetite in spinel, a^{ol}_{fa} is the activity of fayalite in olivine, and a_{SiO_2} is the activity of SiO_2. The activities of components in phases (e.g., activity of fayalite in olivine) are calculated using mineral compositions and activity composition models and a_{SiO_2} estimated by mineral assemblages in a given sample (see discussion below). If K_1, $a^{sp}_{Fe_3O_4}$, a^{ol}_{fa}, and a_{SiO_2} are known, then Eq. (1) can be used to calculate the f_{O_2} of an olivine + spinel assemblage.

For rocks containing olivine, spinel, and orthopyroxene, a_{SiO_2} is calculated through either of the equilibria:

$$\begin{aligned} &Fe_2SiO_4 + SiO_2 = Fe_2Si_2O_6 \\ &\text{fayalite} + SiO_2 = \text{ferrosilite}, \end{aligned} \quad (3)$$

$$\begin{aligned} &Mg_2SiO_4 + SiO_2 = Mg_2Si_2O_6 \\ &\text{forsterite} + SiO_2 = \text{enstatite}. \end{aligned} \quad (4)$$

The equilibrium constant for Eq. (4) (the forsterite–enstatite silica buffer) is:

$$K_4(T,P) = \frac{a^{opx}_{en}[T,P,X]}{a^{ol}_{fo}[T,P,X] * a_{SiO_2}[T,P,X]}, \quad (5)$$

in which a^{opx}_{en} is the activity of enstatite in orthopyroxene and a^{ol}_{fo} is the activity of forsterite in olivine. a_{SiO_2} can be calculated if K_4, a^{opx}_{en}, and a^{ol}_{fo} are known at the P and T of interest. For most peridotite compositions, a^{opx}_{en} and a^{ol}_{fo} are similar to one another and near one. Therefore, a_{SiO_2} in those systems are close to that of the En–Fo buffer.

The combination of Eq. (1) with either Eqs. (3) or (4) forms the foundation for the olivine–orthopyroxene–spinel oxybarometer (e.g, Mattioli and Wood 1988; Wood and Virgo 1989; Ballhaus et al. 1991). Here, we implemented two calibrations of this oxybarometer: that of Ballhaus et al. (1991) (for all samples) and Davis et al. (2017) (for orthopyroxene-bearing samples only, see discussion below). Temperatures used in the calculation were based on the olivine–spinel thermometer of Li et al. (1995). We chose to use this thermometer as it is based on the same elements and minerals (i.e., Fe and Mg contents in olivine and spinel) that are used to calculate f_{O_2}. The two oxybarometer calibrations and our approach to using them are described in more detail here and the results of the calculations given in Table 3.

1. The first calibration is the semi-empirical oxybarometer of Ballhaus et al. (1991) [hereafter abbreviated as B91]. Critically, B91 simplifies the equation used to calculate f_{O_2} by assuming that the effect of ferrosilite activity in orthopyroxene is canceled by the effect of fayalite activity in olivine for samples with high Mg#. The resulting expression for f_{O_2} presented by B91, therefore, does not require knowledge of the coexisting orthopyroxene composition and can be applied to orthopyroxene-undersaturated rocks (although it is not strictly valid in this application). B91 noted that their oxybarometer gave reasonable results for orthopyroxene-undersaturated rocks provided that the calculated f_{O_2} values were corrected for the lower a_{SiO_2} of the system and that corrections rarely exceeded a shift of f_{O_2} by -0.2 log units. Due to the feasibility of applying this calibration to any sample where olivine and spinel compositions are known, we did so for all of our samples. The results of these calculations are given in Table 3 under "Method 1". We note, however, that for orthopyroxene-lacking wehrlites and dunites, the results of these calculations likely represent maxima and therefore we pursued other methods for determining f_{O_2} (see below).
2. Second, for the harzburgites and lherzolites, we applied the olivine–orthopyroxene–spinel oxybarometer following the equations and methods outlined in Davis et al. (2017) (hereafter referred to as D17). Briefly, the D17 method is modified from the equations of Mattioli and Wood (1988) and Wood and Virgo (1989) and the activity of magnetite in spinel ($a^{sp}_{Fe_3O_4}$) is calculated using the MELTS supplemental calculator (Sack and Ghiorso 1991a, b). The results of these calculations are given in Table 3 under "Method 2".

Uncertainties reported in Table 3 are based on 2σ variations in spinel compositions (see Table footnote for discussion of calculations). Variations in olivine composition and temperature considered here result in uncertainties of <0.2 log units. For a full discussion of uncertainties associated with the Method 2 f_{O_2} calculations, see Davis et al. (2017). The greatest uncertainty for orthopyroxene-lacking samples, discussed below, comes from quantification of a_{SiO_2}.

Correction for reduced silica activity

For the samples containing the phase assemblage olivine + spinel ± clinopyroxene (i.e., the wehrlites and

dunites), the f_{O_2} values calculated via B91 (Method 1, as described above) represent maximum estimates, as these samples do not contain orthopyroxene. Therefore, the calculated f_{O_2} values require adjustment for reduced a_{SiO_2}. For example, a decrease in 0.1 log units for a_{SiO_2} results in a corresponding decrease of 0.3 log units in f_{O_2} [see Eq. (2)]).

To account for this, we developed two approaches to calculate a_{SiO_2} in olivine- and clinopyroxene-bearing samples using two silicification equilibria. First, we consider the equilibrium involving forsterite and clinoenstatite:

$$\begin{aligned} &Mg_2SiO_4 + SiO_2 = Mg_2Si_2O_6 \\ &\text{forsterite} + SiO_2 = \text{clinoenstatite}. \end{aligned} \tag{6}$$

The equilibrium constant for Eq. (6) is:

$$K_6(T,P) = \frac{a^{cpx}_{CEn}[T,P,X]}{a^{ol}_{fo}[T,P,X] * a_{SiO_2}[T,P,X]}, \tag{7}$$

where a^{cpx}_{CEn} is the activity of clinoenstatite in clinopyroxene. This equilibrium is attractive as it relates major components of two major phases in olivine- and clinopyroxene-bearing lithologies.

Second, as another alternative to establish a_{SiO_2} in our samples lacking orthopyroxene, we consider the equilibrium involving monticellite and diopside:

$$\begin{aligned} &CaMgSiO_4 + SiO_2 = CaMgSi_2O_6 \\ &\text{monticellite} + SiO_2 = \text{diopside}; \end{aligned} \tag{8}$$

the equilibrium constant for Eq. (8) is

$$K_8(T,P) = \frac{a^{cpx}_{di}[T,P,X]}{a^{ol}_{mo}[T,P,X] * a_{SiO_2}[T,P,X]}, \tag{9}$$

where a^{cpx}_{di} is the activity of diopside in clinopyroxene, a^{ol}_{mo} is the activity of monticellite in olivine, and a_{SiO_2} is the activity of silica referenced to silica glass. Although Ca contents in olivines are perhaps best known for their sensitivity to temperature and use as a geothermometer (Köhler and Brey 1990; Shejwalkar and Coogan 2013), it is also the case that, at a fixed temperature and pressure, Ca contents are also sensitive to a_{SiO_2} via reaction (8) (Stormer 1973; Markl et al. 2001). Therefore, if pressure, temperature, and the coexisting compositions of clinopyroxene and Ca-in-olivine are known, one can calculate a_{SiO_2}. Clearly, there are substantial uncertainties using a minor element abundance to calculate the activity of a major oxide component. However, Ca concentrations in olivine from natural samples indicate that this variable is sensitive to silica activity. For example, olivines from silica-undersaturated volcanic rocks have higher Ca concentrations than olivine in tholeiitic basalts (Stormer 1973). For example, CaO contents in olivines from nephelinites can reach 1.3 wt% (Simkin and Smith 1970; Stormer 1973; Sisson et al. 2009), whereas maximum CaO contents in olivines from tholeiitic basalts are ~ 0.3 wt% (Moore and Evans 1967; Stormer 1973).

Combining equilibrium 1 and 6 or 8, we calculated f_{O_2} for all samples (except dunites) (results are reported in Table 3 under Methods 3 and 4, respectively, and shown in Fig. 5a). (For the three dunite samples we have no constraints on their a_{SiO_2} and therefore treat the f_{O_2} estimates obtained via B91 as a maximum.) Activities of forsterite and monticellite in olivine, clinoenstatite in clinopyroxene, and magnetite in spinel were calculated using the MELTS supplemental calculator which implements the olivine activity-composition model of Hirschmann (1991), the clinopyroxene activity-composition model of Sack and Ghiorso (1994a, b, c), and the spinel activity-composition model of Sack and Ghiorso (1991a, b). Temperatures obtained via olivine–spinel Fe–Mg exchange thermometry of Li et al. (1995) were used to assess Eq. (6). For Eq. (8), Ca-in-olivine temperatures of Shejwalkar and Coogan (2013) (their Eq. 13) were used, as we consider them to best represent the temperature of equilibrium for Ca partitioning between olivine and clinopyroxene.

To verify that reasonable a_{SiO_2} values could be obtained using these alternative equilibria, we first discuss calculated a_{SiO_2} for lherzolite and harzburgite samples where we knew that a_{SiO_2} was near the enstatite–forsterite (En–Fo) buffer. For these samples, we also calculated a_{SiO_2} via Eqs. (3) (enstatite–forsterite) and 4 (ferrosilite–fayalite) using sample average mineral compositions. The results of the four different methods for calculating a_{SiO_2} are shown in Fig. 5b. Calculated a_{SiO_2} via Eq. (3) falls predictably (and reassuringly) on the enstatite–forsterite buffer, whereas those values calculated via Eq. (4) are offset to elevated (by ~ 0.05 to 0.1 log units). a_{SiO_2} values calculated via the clinoenstatite–forsterite (CEn–Fo) equilibrium are offset to lower values than the En–Fo buffer (by 0.12–0.36 log units), and those calculated via the diopside–monticellite (Di–Mo) equilibrium to higher values (by 0.08–0.14 log units). Therefore, the CEn–Fo equilibrium tends to underestimate a_{SiO_2}, whereas the Di–Mo equilibrium overestimates it. Based on this analysis, we consider calculated a_{SiO_2} via the CEn–Fo equilibrium a minimum estimate, whereas that of Di–Mo is a maximum estimate for the remaining orthopyroxene-lacking samples.

Figure 5a displays calculated $\log(a_{SiO_2})$ values for all olivine- and clinopyroxene-bearing samples, as well as various silica activity buffers, including the En–Fo [Eq. (4)] and the Di–Mo [Eq. (8)] buffers. The calculated a_{SiO_2} values via the Di–Mo equilibrium (diamonds) lay along a parallel, though a slightly elevated (by up to 0.14 log units) trend to the En–Fo buffer. We suspect that one reason for this may be that the temperatures used in the calculations are based upon the Ca-in-olivine thermometer of Shejwalkar and Coogan (2013), which in turn is based on orthopyroxene-saturated

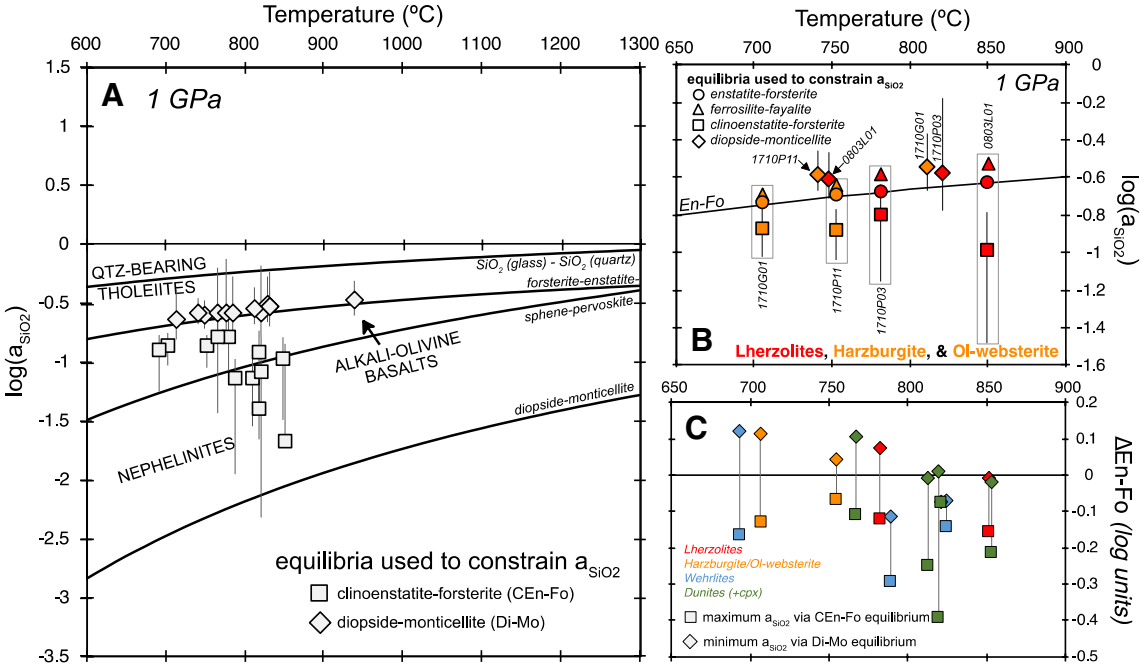

Fig. 5 Summary of methods and estimates of silica activity in studied samples (except dunites). Errors in **A** and **B** represent those reported in Table 3. **a** Calculated $\log(a_{sio_2})$ versus temperature with common silica buffers at 1 GPa. Silica buffers were calculated assuming pure phases (using thermodynamic data of Berman (1988) and the MELTS supplemental calculator) and relative to silica glass (rather than quartz). Calculated a_{sio_2} using clinoenstatite–forsterite (CEn–Fo) equilibria (Eq. 6) are shown as squares and plotted at olivine-spinel Fe–Mg exchange temperatures, whereas the diopside–monticellite (Di–Mo) equilibria (Eq. 8) are shown as diamonds and plotted at Ca-in-olivine temperature estimates (Shejwalkar and Coogan 2013, their Eq. 13). **b** Estimates of $\log(a_{sio_2})$ for olivine–orthopyroxene–spinel-bearing samples (lherzolites and harzburgites) only versus temperature. In addition to CEn–Fo and Di–Mo equilibria, calculated $\log(a_{sio_2})$ values based on forsterite–enstatite (Eq. 4) and ferrosilite–fayalite (Eq. 3) equilibria are shown plotted at olivine–spinel Fe–Mg exchange temperatures. The latter two estimates were calculated using average olivine and orthopyroxene compositions. **c** Calculated best estimate range for $\log(a_{sio_2})$ as represented as log unit difference from the En-Fo buffer (ΔEn-Fo) versus temperature. The range of what is considered the best estimate of $\log(a_{sio_2})$ is defined by the minimum calculated a_{sio_2} using Di–Mo equilibria (based on 2σ variations in Ca contents in olivine) and the maximum a_{sio_2} using CEn–Fo equilibria (based on 2σ variations in Ca and Mg contents in clinopyroxene) (see text for further discussion). Thin grey lines connect calculated a_{sio_2} for individual samples which are plotted at olivine–spinel Fe–Mg exchange temperatures

experiments. Therefore, the use of these temperatures when calculating a_{SiO_2} via Eq. (8) may artificially fix a_{SiO_2} at the En–Fo buffer.

In contrast, the calculated a_{SiO_2} values based on the CEn–Fo equilibrium (squares) are offset to values lower than the En–Fo buffer (again similar to a_{SiO_2} values calculated for the orthopyroxene-saturated samples). In addition, they typically show larger associated errors. The larger uncertainties are related to intrasample variations in the CaO and MgO contents of clinopyroxene. At clinopyroxene CaO contents greater than ~25 wt%, the mole fraction of clinoenstatite decreases below ~0.02 and the corresponding $\log(a^{cpx}_{CEn})$ begins to drop dramatically and non-linearly with increasing CaO content (Fig. S2), which propagates into larger uncertainties on calculated a_{SiO_2} values. The average calculated a_{SiO_2} values [via CEn–Fo equilibria, Eq. (6)] for 50% of the samples yield reasonable values within the field of alkali-olivine basalts (Fig. 5a); however in the other samples, they fall below the sphene–perovskite buffer in the field of nephelinites. These calculated a_{SiO_2} are clearly too low, as a_{SiO_2} values appropriate for nephelinitic lavas are not expected for Talkeetna arc magmas.

In summary, we consider a_{SiO_2} values calculated via the Di–Mo equilibrium maximum estimates and those calculated via the CEn–Fo equilibrium minimum estimates. Proceeding with this assumption, we take the maximum a_{SiO_2} values determined via CEn–Fo equilibrium (based on 2σ intrasample variations in clinopyroxene CaO and MgO contents) and the minimum a_{SiO_2} values determined via Di–Mo equilibrium (based on 2σ intrasample variations in olivine Ca contents) as a range of best estimates for a_{SiO_2} in the samples lacking orthopyroxene (Fig. 5c). In situations where the errors for these two methods overlap, we simply consider calculated a_{SiO_2} using sample average mineral compositions as the best bracketing values. For the orthopyroxene-bearing samples (red and orange symbols in Fig. 5c), the $\log(a_{SiO_2})$ best estimate brackets encompass the En–Fo buffer. For orthopyroxene-lacking samples, the $\log(a_{SiO_2})$ best estimate

brackets are generally lower than those of the En–Fo buffer (as expected), but range between ΔEn–Fo = + 0.11 and − 0.39 (blue and green symbols in Fig. 5c).

Preservation of magmatic f_{O_2} in cumulates

f_{O_2} during cumulate solidification

The composition of "primocrysts" (or minerals that form the framework for cumulates) should reflect the f_{O_2} of the initial primary magma from which the crystallized. However, after accumulation of the primocrysts, interstitial melt may be trapped between them. As the interstitial melt cools and solidifies, the textures and compositions of mesocumulate and orthocumulate minerals evolve (Jackson 1961; Henderson 1970; Cameron 1975; Roeder and Campbell 1985; Bell and Claydon 1992). The nature of intercumulus crystallization depends on the permeability of the cumulate framework. During adcumulate formation (> 93% primocrysts) and conditions of high permeability, the evolving intercumulus liquid can maintain communication with liquid from the main magma reservoir and therefore perfect adcumulates should only contain primocrysts with essentially unzoned overgrowths (Sparks et al. 1985; Tait et al. 1984; Kerr and Tait 1986; Tait and Jaupart 1992; Holness et al. 2017). In contrast, in systems with high porosity, but low permeability, meso- (75–93% primocrysts) to orthocumulus (< 75% primocrysts) formation will occur resulting in primocrysts with zoned overgrowths and evolved intercumulus phases resulting from crystallization of trapped liquid (Wager et al. 1960; Humphreys 2009).

Of particular concern for this study is the potential that crystallization of trapped interstitial liquid in the cumulates drives a change in f_{O_2} and variations in mineral chemistry not reflecting that of the primary magma (c.f. Roeder and Campbell 1985). For example, in a study of chromites in olivine adcumulates, mesocumulates, and orthocumulates from the Jimberlana intrusion (Australia), Roeder and Campbell (1985) found the chromites (< 50 µm in diameter) in adcumulates and mesocumulates had restricted compositional ranges, whereas orthocumulate chromites varied in composition from that found in the ad- and mesocumulates to compositions with higher Fe, Ti, and Fe^{3+} contents. This observation in the orthocumulates was interpreted as evidence for mineral equilibration with intercumulus liquid that became more oxidizing upon cooling. Thus, whether variations in f_{O_2} during cumulate solidification will be recorded in the cumulate mineral is dependent on the relative mass of the interstitial melt versus primocrysts. If primocrysts dominate, as in the adcumulates studied here, then changes in f_{O_2} will likely be recorded only in minor rims on the primocrysts. In contrast, if the cumulates represent greater percentages of trapped liquid, the evolving f_{O_2} may be recorded by thicker rims.

Our f_{O_2} calculations are based on mineral core analyses, thus limiting the chance for overprinting due to interstitial liquid crystallization. In addition, there are several lines of evidence that suggest that cumulates are adcumulate in character and did not have significant trapped intercumulus liquid. (1) Most are near-monomineralic, dominated by olivine (> 90%; i.e., dunites and clinopyroxene-bearing dunites). The exceptions to this are spinel-rich dunites and wehrlites, which have heteradcumulate to adcumulate textures (Fig. 2b, c). (2) Core-to-rim compositional zoning is absent in olivines. Spinels are also unzoned, except in three samples (1709P02, 1805L01, and 1710P12; see discussion above) where a 40–60 µm rim is observed (on grains 100 s of µm in diameter). (3) Although bulk rock trace element chemistry is not available for most of the samples, other dunites from the Tonsina area have extremely low incompatible trace element concentrations (e.g., $\sum$REE < 0.1 ppm; Kelemen et al. 2003) consistent with lithologies dominated by olivine and little, if any, incompatible element-enriched trapped liquid.

Subsolidus processes and their effect on calculated f_{O_2}

As the samples investigated in this study have experienced subsolidus cooling and, to some degree, alteration, it is necessary to assess the effect of these processes on the calculated oxygen fugacities. In a study of variably altered seafloor peridotites, Birner et al. (2016) demonstrated that high degrees of serpentinization did not affect the mineral parameters such as forsterite number in non-serpentinized olivine, iron site occupancy in orthopyroxene, or the Fe^{3+}/Fe^{T} in spinel. The constancy in f_{O_2} calculated based on olivine–orthopyroxene–spinel oxybarometry [e.g., Eq. (1)] even at high degrees of alteration led them to suggest that low-temperature serpentinization did not affect the f_{O_2} recorded in the mineral compositions. Therefore, we do not believe low-temperature serpentinization influenced our calculated f_{O_2} even though a number of the samples contain serpentine (e.g., Fig. 2a, b, Table 1).

Higher temperature re-equilibration of mineral compositions during cooling can also affect the f_{O_2} recorded in magmatic rocks (e.g, Cameron 1975; Clark 1978; Wilson 1982; Lindsley and Frost 1992; Ballhaus 1993; Woodland et al. 1996; Birner et al. 2018). Diffusion of elements between minerals proceeds until the closure temperature of a specific element is reached (e.g, Dodson 1973). For example, Fe^{2+} and Mg^{2+} exchange between olivine and spinel will continue until relatively low temperatures (~ 700 to 800 °C) due to rapid diffusivity and low closure temperature of this exchange system (Jurewicz and Watson 1988; Van Orman and Crispin 2010). Birner et al. (2018) quantitatively assessed the effect of subsolidus exchange reactions on the

f_{O_2} preserved in lherzolites and harzburgites. Their calculations considered Fe^{2+}–Mg^{2+} diffusion between olivine and spinel, as well as Al^{3+}–Cr^{3+} diffusion between spinel and orthopyroxene as a function of temperature using the model presented by Voigt and von der Handt (2011). They found that subsolidus exchange reactions increased calculated f_{O_2} by 0.15–0.20 log units over 120 °C of cooling. In contrast, slowly cooled peridotites exemplified by orogenic massifs demonstrate consistently lower f_{O_2} (~FMQ − 1; (Woodland et al. 1992; 2006; Canil and O'Neill 1996) as compared to abyssal peridotites (~FMQ; Bryndzia and Wood 1990; Birner et al. 2018), suggesting a decrease in f_{O_2} during cooling. Canil and O'Neill (1996) suggested that growth of spinel during cooling, resulting in lower Fe^{3+} in spinel, could result in lower calculated f_{O_2} for orogenic massifs. In this scenario, slowly cooled intrusive rocks likely preserve a minimum f_{O_2}.

In dunites (± clinopyroxene) similar to those studied here, olivine–spinel Fe^{2+}–Mg^{2+} exchange is important, while Al^{3+}–Cr^{3+} exchange is limited. Without an external f_{O_2} buffer and assuming constant modal percentages of minerals, cooling will decrease the Fe^{2+} content of olivine in dunites, lowering the proportion of fayalite, without affecting the proportion of magnetite in spinel, and thus increasing f_{O_2}. In practice, however, dunites generally have large olivine/spinel ratios so that Fe^{2+}–Mg^{2+} exchange during cooling has a large effect on spinel Mg# coupled with a barely discernible effect on olivine composition or increases in Mg# limited to olivine rims. However, two spinel-rich dunites (2814L09 and 2808L04) have elevated Mg# (95.3 and 93.0, respectively) as compared to that expected for olivine crystallizing from primary melts (~90), suggesting that Fe^{2+}–Mg^{2+} exchange with spinels may have been extensive in these samples. To assess the effect on inferred f_{O_2} from this process, we modeled the cooling of four dunites (± clinopyroxene) assuming temperature-dependent Fe^{2+}–Mg^{2+} exchange between olivine and spinel (Li et al. 1995; Fig. S3). We found that cooling from 1100 to 800 °C resulted in an increase of 0.30–0.35 log units, consistent with the calculations of Birner et al. (2018). (Although orthopyroxene is not present in the majority of samples studied here, Al^{3+}–Cr^{3+} exchange between clinopyroxene and spinel may have affected our samples. However, at this time, a detailed understanding of ferric iron partitioning between spinel and clinopyroxene is not available to fully model the subsolidus evolution of peridotites.)

Lastly, although subsolidus cooling and diffusion of Ca have almost certainly modified the Ca contents of olivine in the samples, the relative a_{SiO_2} of the mineral assemblage was likely buffered at values equivalent to those at the time of initial crystallization (Carmichael et al. 1970).

Calculated f_{O_2} and comparison to previous estimates for the Talkeetna Arc

Calculated f_{O_2} values using the B91 calibration (Method 1, applied to all samples), the D17 approach (Method 2, only applied to orthopyroxene-bearing samples), and combining equilibrium 1 and 6 (Method 3) or 1 and 8 (Method 4) (applied to all olivine- and clinopyroxene-bearing samples) are reported in Table 3 and shown in Fig. 6. The f_{O_2} calculated via Method 1 is between FMQ + 0.3 and + 2.1, and in the majority of samples (75%) are higher (by ~0.2 to − 1.8 log units) than those calculated via Methods 2–4. This is expected as Method 1 likely overestimates a_{SiO_2} in orthopyroxene-lacking samples by fixing it near the En–Fo buffer. For the harzburgites and lherzolites we take the f_{O_2} values calculated via Method 2 as our best estimates. Using this method, the harzburgites both yielded f_{O_2} values of FMQ + 1.3 (± 0.2), whereas the lherzolites yielded f_{O_2} values of FMQ + 0.8 (± 0.2 to 0.4). For olivine and clinopyroxene samples, we consider the averages of f_{O_2} values calculated via Methods 3 and 4 as our best estimates and therefore discuss these values from here on. These f_{O_2} values varied between FMQ + 0.4 and + 2.3.

Although there is a two-order of magnitude variation in our f_{O_2} estimates, the calculated f_{O_2} values do not vary systematically by locality or chemical indices of differentiation (e.g, Mg# in olivine). One clinopyroxene-bearing dunite from Eklutna (2808L04) is an outlier, recording an average calculated f_{O_2} value of FMQ + 2.3, whereas calculated f_{O_2} values of all other samples fall between FMQ + 0.4 to FMQ + 1.6 (Fig. 6a). For the true dunites (i.e., no clinopyroxene present) we consider the f_{O_2} values calculated via Method 1 a maximum estimate and show their values as light green bars at the top of Fig. 6a. These maximum f_{O_2} estimates are FMQ + 0.8, + 1.1, and + 1.2.

The calculated f_{O_2} values of FMQ + 0.4 to FMQ + 1.6 (not including the one outlier of FMQ + 2.3) for the lower crustal ultramafic cumulates are lower (by 1–2 log units) than previous estimates based on thermodynamically calculated equilibrium mineral assemblages from bulk rock gabbronorite compositions from Talkeetna (Behn and Kelemen 2006). Specifically, the quartz–olivine–garnet-free mineral assemblage found in most Talkeetna gabbronorites could only be reproduced in thermodynamic calculations with f_{O_2} between NNO + 1 (~FMQ + 2) and NNO + 3 (~FMQ + 4) at pressures between 0.7 and 1.0 GPa. This relatively narrow range in f_{O_2} for olivine-free gabbronorites predicted from mineral equilibria arises essentially because olivine is unstable relative to orthopyroxene + magnetite at $f_{O_2} >$ NNO + 1, and quartz is not stable relative to orthopyroxene + magnetite at $f_{O_2} <$ NNO + 3. The difference between the f_{O_2} estimates for the ultramafic rocks in this study (with clinopyroxene Mg# of 87.8–95.6) and the structurally higher and more

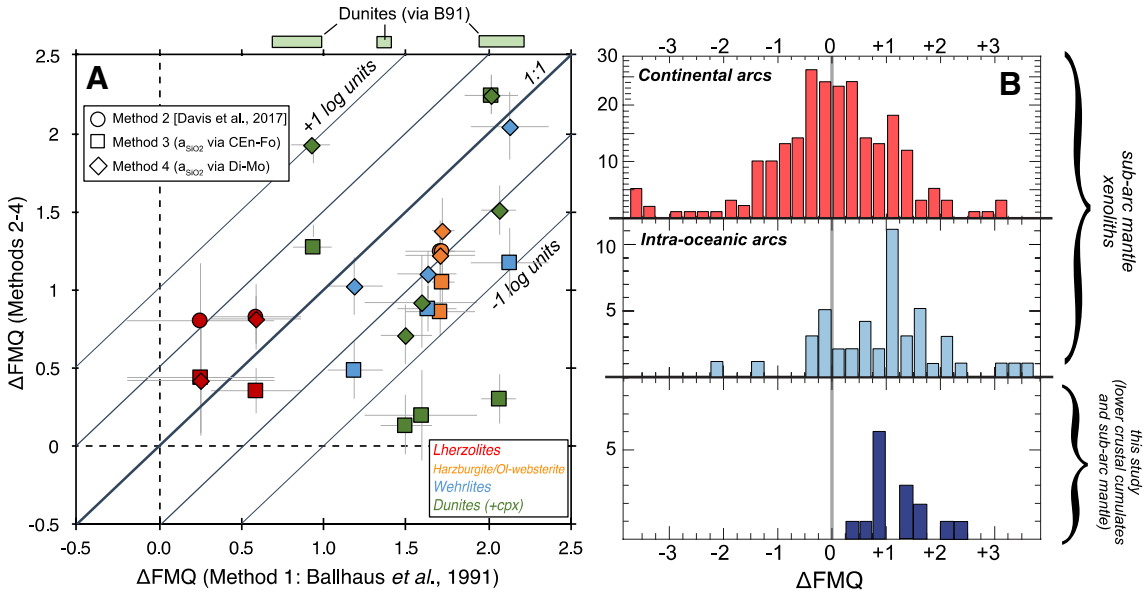

Fig. 6 Calculated oxygen fugacity values of Talkeetna arc lower crustal cumulates and residual mantle. **a** Comparison of calculated oxygen fugacity values relative to the fayalite–magnetite–quartz buffer (FMQ) using Methods 2-4 versus that of Ballhaus et al. (1991) (see text for full description of methods). Error bars on estimates represent uncertainties associated with intrasample variation in spinel compositions. **b** Histograms of oxygen fugacity values (ΔFMQ) for xenoliths from arc lavas based on compilation of Arai and Ishimaru (2008) (see references therein) and the Talkeetna arc (this study). Localities included for continental arcs are Japan, Luzon-Taiwan arc, Cascades, Mexico, and Kamchatka and for oceanic arcs are Vanuatu and Lesser Antilles

evolved gabbronorites (average Talkeetna gabbronorite bulk rock Mg# = 58 ± 1, 1σ; Kelemen et al. 2003 and clinopyroxene Mg# = 76.5 ± 3.4, 1σ; Greene et al. 2006) could be due to either the relatively large uncertainties associated with both sets of f_{O_2} estimates (± 0.5 to ± 1 log units) or an actual reflection of varying f_{O_2} with depth in the Talkeetna arc crust, and/or a substantial increase in f_{O_2} during subsolidus cooling of the gabbronorites. The gabbronorites could have crystallized at a higher f_{O_2} as compared to the ultramafic cumulates. For example, crystallization of abundant Fe^{2+}-bearing olivine and pyroxenes at the base of the arc producing the ultramafic cumulates could preferentially enrich the remaining melt in Fe^{3+}, leading to an increase in f_{O_2} with progressive crystallization (Presnall 1966; Sato 1978; Carmichael and Ghiorso 1990; Kelley and Cottrell 2012; Ulmer et al. 2018). In addition, fractionation of garnet, which is observed in some of the gabbronorites, and may have been common in dense lithologies that foundered into the mantle (c.f., Behn and Kelemen 2006; Jull and Kelemen 2001), could also produce an increase in f_{O_2} (Tang et al. 2018).

We estimate the magnitude and direction of f_{O_2} variation expected during early crystallization–differentiation of the analyzed lithologies at the base of the Talkeetna arc. First, we calculated bulk cumulate compositions for an average dunite, dunite + clinopyroxene, and wehrlite using average modal percentages (converted to mass percentages) and mineral compositions. Bulk cumulate compositions are given in Table 4. We used an average primary melt composition for Talkeetna from Greene et al. (2006) (average of calculated primary magmas in their Table 10) with $Fe^{3+}/Fe^{T} = 0.15$, appropriate for ~ FMQ at 1 GPa and 1200 °C [using Eq. (7) and values in Table 7 of Kress and Carmichael 1991; see Table 4]. We then stepwise subtracted the bulk cumulate compositions in 1% melt increments, accounting for decreasing melt mass according to equations of Jagoutz (2010). 5% dunite, 5% clinopyroxene-bearing dunite, and 5% wehrlite crystallization (consistent with Fe^{2+}/Mg equilibrium partitioning between evolving melt and cumulus olivine compositions) result in an increase in melt Fe^{3+}/Fe^{T} ratio from 0.15 to 0.18, corresponding to ~ 0.5 log unit increase in f_{O_2} (at 1 GPa and 1200 °C). Notably, the cumulate lithologies are olivine dominated with low calculated bulk Fe^{3+}/Fe^{T} ratios of ~ 0.02. Clinopyroxene compositions on average have Fe^{3+}/Fe^{T} ratios (based on assumptions of stoichiometry and charge balance) of 0.21; however, they do not dominate the cumulus assemblage and clinopyroxene reaches a maximum of 22 modal percent even in the most clinopyroxene-rich wehrlite (1710P12). Crystallization of such cumulates, even without quantitative modeling, therefore is expected to increase the Fe^{3+}/Fe^{T} ratio of the residual melts.

Comparison to f_{O_2} estimates of arc peridotites and volcanic rocks

The range of f_{O_2} preserved in the Talkeetna sub-arc mantle and primitive, ultramafic cumulates (FMQ + 0.5 to 2.5) is

Table 4 Primary melt and cumulate compositions used in fractional crystallization modeling

	Primary Talkeetna melt	Dunite	Dunite + clinopyroxene	Wehrlite
SiO_2	49.99	39.12	39.15	41.23
TiO_2	0.65	0.02	0.03	0.04
Al_2O_3	14.43	0.69	0.66	0.95
Cr_2O_3	0.08	2.31	1.99	1.18
FeO	6.36	9.98	10.32	10.44
Fe_2O_3	1.25	0.45	0.43	0.43
MnO	0.24	0.17	0.17	0.17
MgO	11.94	47.12	46.03	41.43
CaO	11.64	0.00	0.59	3.73
Na_2O	1.67	0.02	0.02	0.03
K_2O	0.72	–	–	–
P_2O_5	0.13	–	–	–
Total	99.09	99.87	99.38	99.64
molar Mg#	0.74	0.89	0.89	0.88
Fe^{3+}/Fe^{T}	0.10	0.02	0.021	0.019
Mass % of cumulate minerals				
Olivine	–	0.951	0.933	0.813
Spinel	–	0.049	0.043	0.033
Clinopyroxene	–	0.000	0.024	0.153
Samples included in average	Calculated primary melt compositions given in Table 10 of Greene et al. (2006) with FeO/Fe_2O_3 adjusted for FMQ at 1.0 GPa and 1200 °C	1709P02, 2808L06, 2809L03	1802L07, 1805L01, 2809L02, 2814L07	1710P12, 2813L01

in agreement with those previously determined for peridotite xenoliths from oceanic and continental arcs (Fig. 6b, Brandon and Draper 1996; Blatter and Carmichael 1998; Parkinson and Arculus 1999; Parkinson et al. 2003; Bryant et al. 2007; Arai and Ishimaru 2008). The average f_{O_2} estimated for oceanic arc peridotites is FMQ + 1.1 (Fig. 6b), the same (within error) as that of the Talkeetna lower crust and uppermost mantle. Another useful comparator dataset for the Talkeetna arc is that of the accreted Kohistan arc (Pakistan) which is another type locality for an accreted intra-oceanic arc section (e.g., Jagoutz and Kelemen 2015). Although no estimates of f_{O_2} of cumulate rocks from primary arc magmas at the base of the Kohistan arc exist, f_{O_2} for three sub-arc mantle samples have been determined previously using the B91 method (Williams et al. 2004; 2005). Calculated f_{O_2} for these samples were FMQ + 1.4, + 2.1, and + 2.3, again broadly in agreement with that of the Talkeetna lower crustal estimates though slightly more elevated on average.

In addition, the range of f_{O_2} determined for basaltic glasses and melt inclusions from the Mariana arc volcanoes of FMQ + 1.0 to FMQ + 1.6 (Kelley and Cottrell 2009; Brounce et al. 2014), and of FMQ − 1 to FMQ + 3.5 for silicic arc volcanic rocks (Carmichael 1991; Sisson et al. 2005) is also broadly consistent with that of the Talkeetna primary arc melts, consistent with the hypothesis that Fe^{3+}/Fe^{T} ratios in typical arc volcanic rocks record f_{O_2} representative of their mantle source region. In summary, our data reinforce the conclusions of previous authors that some arc lavas and mantle peridotite xenoliths preserve similar f_{O_2} that reflect f_{O_2} in their mantle source regions elevated above that of MORB mantle.

Redox-sensitive trace element ratios in Talkeetna volcanic rocks

With f_{O_2} calculated for the Talkeetna sub-arc mantle and primitive, lower crustal cumulates, we can now test whether redox-sensitive trace element ratios in volcanic rocks from the Talkeetna arc reflect the f_{O_2} of their source region and primary basalts generated in the arc. Several trace element ratios involving V have been proposed as oxybarometers (e.g., Ti/V, V/Sc, V/Ga, V/Yb, V/Y) (Shervais 1982; Li and Lee 2004; Lee et al. 2005; Mallmann and O'Neill 2009; Laubier et al. 2014). The premise for use of these ratios stems from the fact that V is an incompatible, multivalent element with mineral–melt partitioning behavior that is strongly dependent on f_{O_2} (e.g, Canil 1997; Canil and Fedortchouk 2000; Canil 2002; Mallmann and O'Neill 2009; Mallmann & O'Neill 2013). In olivine, pyroxenes, and spinel, V becomes more incompatible with increasing f_{O_2}. Therefore, partial melts of the mantle produced under higher f_{O_2} conditions will have higher V concentrations than

those produced under lower f_{O_2} conditions (assuming similar source compositions and degree of partial melting). This behavior of V has led to the application of V/Sc (Li and Lee 2004; Lee et al. 2005; Mallmann and O'Neill 2009), V/Ga (Mallmann and O'Neill 2009), and V/Yb (Laubier et al. 2014) ratios in basalts as redox proxies for f_{O_2} in their mantle source regions. In addition, these ratios have been suggested to be resistant to the effects of assimilation, fractional crystallization (at high bulk rock MgO concentration, generally > 6 wt%), and alteration.

Similarities in these ratios between arc volcanic rocks and MORBs have led to the interpretation that their mantle sources also have similar f_{O_2}, which is inconsistent with f_{O_2} calculated via oxybarometry on arc mantle xenoliths and Fe^{3+}/Fe^{T} ratios, summarized above. For example, similar V/Sc and V/Ga ratios in MORB and arc basalts have led to the suggestion that the f_{O_2} in their mantle source regions (relative to a buffer) is similar and within one log unit of FMQ (Lee et al. 2005; Mallmann and O'Neill 2009). The Talkeetna paleo-arc presents a unique opportunity to simultaneously quantify redox-sensitive trace element ratios in volcanic rocks and the f_{O_2} of the sub-arc mantle and the primitive magmas that crystallized at the base of the arc crust in the same magmatic arc. These observations can help us understand whether redox-sensitive trace element ratios in lavas faithfully reflect f_{O_2} in their mantle sources. In Fig. 7, we compare V/Sc ratios in MORBs, arc volcanic rocks, and Talkeetna arc volcanic rocks. The compilation of Talkeetna arc volcanic rocks was screened to only include aphyric or plagioclase-phyric basalts with bulk rock MgO contents between 6 and 12 wt% ($n = 20$; Kelemen et al. 2003; Clift et al. 2005; Greene et al. 2006). This was done, following previous workers (e.g., Lee et al. 2005; Stolper and Bucholz 2019) to ensure that the samples represent liquids that have mainly experienced olivine fractionation, which should not affect the V/Sc ratios of the bulk rock. The average V/Sc ratio of the Talkeetna arc volcanic rocks is 6.69 ± 1.61 (2σ) (Fig. 7), similar to those previously compiled for MORB and some arc volcanic rocks (Lee et al. 2005; Stolper and Bucholz 2019). Note that while the mode of V/Sc in arc volcanic rocks is similar to that of MORB, the distribution of arc V/Sc values (red and blue curves in Fig. 7) is asymmetric and skews to higher values than that of MORB (green curves in Fig. 7).

To interpret V/Sc ratios, forward trace element partial melting models of the mantle that incorporate the redox-sensitive V partition coefficients are used (e.g, Lee et al. 2005; Prytulak et al. 2017). For example, the gray curves in Fig. 8a show results calculated using the method of Lee et al. (2005) for non-modal batch partial melting of a spinel lherzolite, using partition coefficients from Canil (2002) and an initial source V/Sc ratio of 4.9 (V = 79 and Sc = 16.3). Typically, modeled V/Sc ratios at a melt fraction of 10%

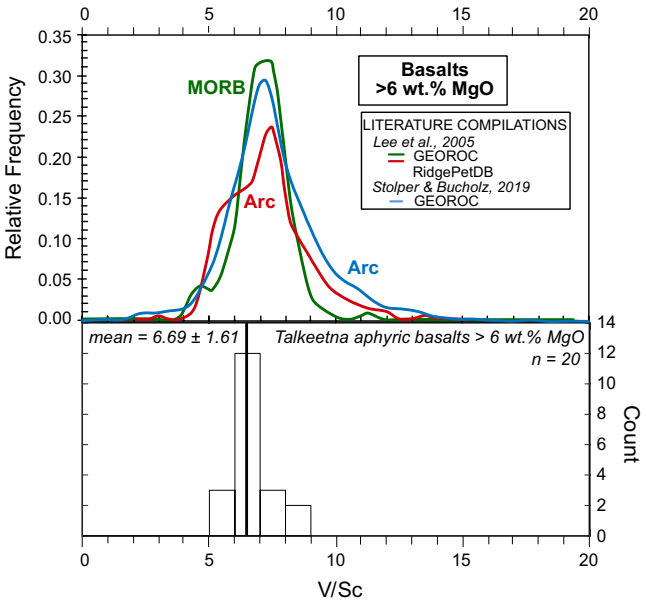

Fig. 7 Whole-rock V/Sc ratios for arc and MORBs (upper panel), as well as the Talkeetna arc (lower panel). Upper panel is after Figure 10b in Lee et al. (2005) and shows normalized frequency distributions for the literature data compiled in that study from the GEOROC and RidgePetDB databases. In addition, an updated compilation of modern arc volcanic rocks from the GEOROC database from Stolper and Bucholz (2019) is shown for comparison. Note the tailed distribution for arcs towards higher V/Sc values. The lower panel is a histogram for Talkeetna lavas ($n = 20$ samples) with MgO between 6–12 wt.% from Clift et al. (2005), Greene et al. (2006), and Kelemen et al. (2003)

have been used to compare to volcanic rock data, as this is the best estimate for degree of melting at mid-ocean ridges. The gray iso-fugacity curves in Fig. 7b and a melt fraction of 10% suggest that the mantle source region for the Talkeetna arc volcanic rocks had on average an f_{O_2} near FMQ − 0.5.

However, partial melting models involve a number of assumptions, including source mineralogy, degree and style of melting, bulk source trace element composition, and choice of partition coefficients (Lee et al. 2005; Prytulak et al. 2017; Wang et al. 2019). In particular, these models are highly sensitive to both source V/Sc ratios and degree of melting. To explore this sensitivity, we follow the modeling approach of Prytulak et al. (2017) to capture the expected variations in V/Sc as a function of f_{O_2} and degree of melting for a previously depleted arc source region (i.e., in the back arc). Briefly, V/Sc ratios used the non-modal melting equations (Shaw 1970) for spinel lherzolite melting reaction coefficients (Kinzler 1997). Forward modeling of melt V and Sc concentrations was calculated at 1% melting intervals, and V and Sc mineral–melt partition coefficients are from Mallmann and O'Neill (2009). In addition, although f_{O_2} can both increase and decrease during peridotite partial melting depending on the mode of melting (e.g, isobaric v.

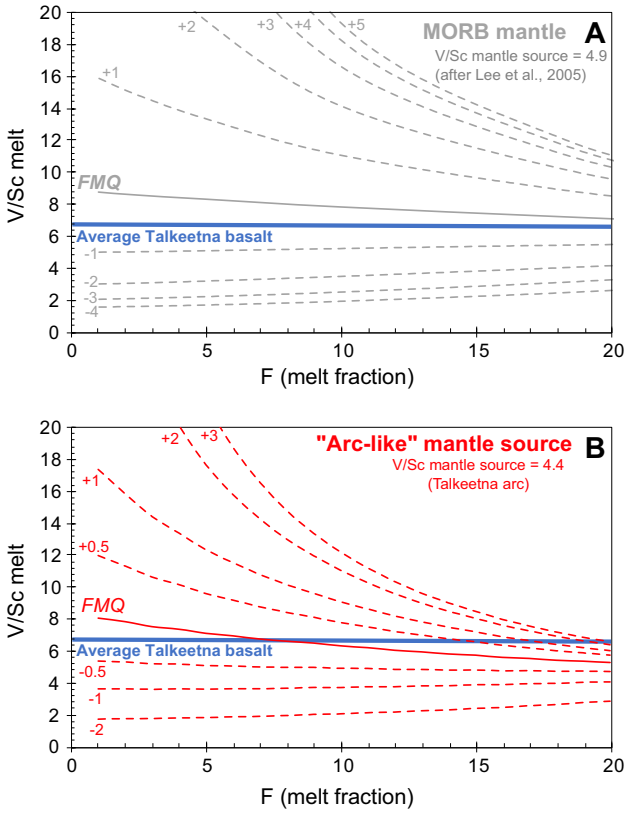

Fig. 8 V/Sc ratios in partial melts of a spinel lherzolite as a function of melt fraction (x-axis) and oxygen fugacity (labeled curves). The blue line and shaded area indicate the average V/Sc ratio (±2σ) of Talkeetna volcanic rocks (> 6 wt.% MgO) as shown in panel A. In A, V/Sc ratios were calculated following method of Lee et al. (2005) and is the same as their Figure 6a (see text for more details). An initial mantle source V/Sc ratio of 4.9 was assumed. In B, V/Sc ratios were calculated using the non-modal melting equations of Shaw (1970) and the spinel-lherzolite melting reaction coefficients of Kinzler (1997) from her 1.5 GPa experiments L134–L138 (0.13opx + 0.89cpx + 0.12sp = liquid + 0.13ol). An initial mantle source V/Sc ratio of 4.4 was assumed (see text for details). At 15–20% melting, the average V/Sc ratio of Talkeetna volcanic rocks corresponds to oxygen fugacity values between FMQ +0.5 and FMQ +2

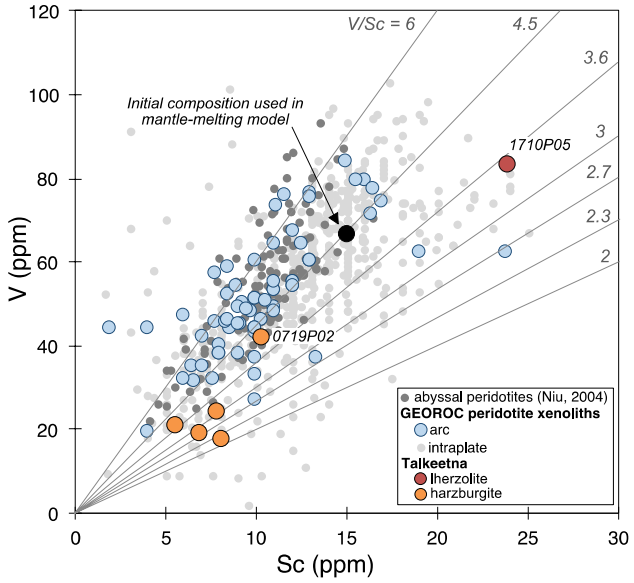

Fig. 9 V versus Sc (ppm) in spinel lherzolites and harzburgites. Data from arc (blue dots) and continental and oceanic intraplate (light grey dots) volcanic rocks are from the GEOROC database. Abyssal peridotite data (dark grey dots) are from the compilation of Niu (2004). Talkeetna bulk-rock peridotite data (orange and red circles) is from Kelemen et al. (2003) and do not correspond to any of the samples analyzed in this paper. V was determined via X-ray fluorescence and Sc via inductively coupled plasma mass spectrometry. 0719P02 is identified as the "least depleted" harzburgite due to its elevated V and Sc concentrations as compared to other harzburgites. 1710P05 is the only lherzolite from Talkeetna analyzed for bulk-rock chemistry and is shown for reference. The filled black circle indicates composition of mantle used in mantle-melting model (V/Sc = 4.4). Grey lines indicate isopleths for different V/Sc ratios

decompression, Gaetani 2016), this is not accounted for in our modeling.

An initial "arc-like" mantle source was calculated after 10% depletion of a "MORB-like" mantle source (olivine–orthopyroxene–clinopyroxene–spinel modal percentages of 60–20–15–5), resulting in a residual modal mineral abundance 66.3% olivine, 20.6% orthopyroxene, 8.7% clinopyroxene, and 4.4% spinel. Although it is uncertain what the initial mantle source V/Sc ratio was for the Talkeetna paleo-arc, residual harzburgites from Tonsina have an average bulk rock V/Sc ratio of 3.2 ± 0.8 (1σ, $n = 5$; Kelemen et al. 2003; orange dots in Fig. 8). The least depleted harzburgite (sample 0719P02) has initial concentrations of V = 42 ppm and Sc = 10.3 ppm with a bulk V/Sc ratio of 4.1 (Fig. 9; Kelemen et al. 2003). The other four previously analyzed samples have lower and more similar V and Sc concentrations with an average V/Sc ratio of 2.9 ± 0.64 (1σ), with the lowest V/Sc ratio in an individual harzburgite of 2.2 (Fig. 9).

Using the model described above at an f_{O_2} of FMQ + 0.8, we calculate a hypothetical initial mantle starting composition assuming the residual mantle after 15% partial melting had a V/Sc ratio of 2.2. This requires the initial sub-arc source mantle to have a V/Sc ratio of 4.4, similar to both the least depleted harzburgite (0719P02), as well as calculated V/Sc ratios after 5–10% depletion of "MORB-like" mantle at FMQ (initial V/Sc of 4.9). We therefore assume an initial mantle source V/Sc ratio of 4.4 (using V = 66.5 ppm and Sc = 15.1 ppm; Fig. 9) based on calculated depletion of a "MORB-like" mantle. This value is within the range of V/Sc values observed for bulk rock lherzolites and harzburgites xenoliths from arcs which average V/Sc ratio of 4.9 ± 1.0 (1σ, Fig. 9). Prior depletion of arc sources may occur during back-arc melt generation events or general depletion of the upper mantle during MORB formation, leaving behind refractory material that is unable to melt during adiabatic

decompression, but can partially melt beneath arcs due to hydrous flux melting.

Two observations are immediately obvious from our modeling exercise. First, and predictably, lowering the source V/Sc ratio (through prior depletion) results in a decrease in the V/Sc ratios of the partial melts (Fig. 8b). A subtler effect of mantle depletion is the lower modal abundance of clinopyroxene which will decrease the bulk peridotite partition coefficient for Sc. This in turn causes the bulk partition coefficient for V/Sc to be closer to 1, resulting in partial melts that have V/Sc ratios more similar to their source regions. Second, at higher degrees of melting, the calculated curves for different f_{O_2} converge, and V/Sc ratios become less sensitive to f_{O_2} in the mantle source (Fig. 8). These two factors are critical when interpreting arc volcanic rocks data due to the generally higher degree of mantle melting beneath arcs (e.g, up to 15–20%, Stolper and Newman 1994; Kelley et al. 2006) compared to mid-ocean ridges (~ 10%, Bottinga and Allegre 1976) and/or the fact that many arc magmas appear to be generated from previously depleted source regions (Woodhead et al. 1993; Bacon et al. 1997; Grove et al. 2002; Nebel et al. 2015). Using a more depleted source region with a V/Sc ratio of 4.4 and a melt fraction of 15–20%, the average V/Sc ratios of Talkeetna basalts is consistent with f_{O_2} of FMQ + 0.5 to + 2.0 (Fig. 8b). This modeling exercise suggests that V/Sc ratios of volcanic rocks may be interpreted in the context of mantle source region f_{O_2} provided that the degree of mantle melting and source V/Sc are known, (though at high degrees of melting the sensitivity of V/Sc to f_{O_2} decreases significantly). Although we do not consider the effect of temperature on V mineral–melt partitioning, V becomes more compatible in olivine, pyroxenes, and spinel at lower temperature, which could also serve to produce similar V/Sc ratios in arc basalts generated during low-temperature hydrous flux melting and comparatively high-temperature mid-ocean ridge basalts (Wang et al. 2019). Importantly, similarities in basalt V/Sc ratios do not necessarily imply similar f_{O_2} in their mantle sources.

Conclusions

Our results provide the first comparison of (A) f_{O_2} in the sub-arc mantle and primitive, cumulate rocks based on olivine–spinel oxybarometry, and (B) V/Sc ratios in volcanic rocks from the same locality. Our olivine–spinel-based oxybarometry calculations suggest that f_{O_2} in the sub-arc mantle and primary arc magmas (FMQ + 0.4 to + 2.3) of the Talkeetna arc, while heterogeneous, are, on average, higher than in the MORB mantle source. Our calculated f_{O_2} for primary arc magmas are further consistent with conclusions based upon Fe^{3+}/Fe^{T} ratios in submarine arc glasses and olivine-hosted melt inclusions, sub-arc mantle xenoliths, and silicic arc lavas. With that said, our observations do not preclude oxidation during crustal processes (e.g, crystallization, assimilation, and/or degassing). In addition, our analysis of V/Sc ratios in Talkeetna basalts and their sensitivity to assumptions in model parameters suggest that the similarity of V/Sc ratios in some arc volcanic rocks and mid-ocean ridge basalts does not require that they have source regions with similar f_{O_2}. While V/Sc ratios are sensitive to the f_{O_2} of mantle source regions, it is important to interpret V/Sc and other redox-sensitive trace element ratios in volcanic rocks in the context of detailed modeling where the degree of partial melting and mantle source V/Sc are known.

Acknowledgements Samples used in this study were collected during fieldwork supported by NSF EAR grant #9910899 (PI P. Kelemen). We thank B. Wood for kindly providing spinel standards, C. Lee for sharing his thoughts and insights into modeling V/Sc ratios, conversations with E. Stolper, and C. Ma for assistance with electron microprobe analyses. Thoughtful reviews by T. Sisson and D. Canil helped to clarify and strengthen the manuscript.

References

Adams GE, Bishop FC (1986) The olivine—clinopyroxene geobarometer: experimental results in the CaO–FeO–MgO–SiO_2 system. Contrib Mineral Petrol 94(2):230–237

Amato JM, Rioux ME, Kelemen PB, Gehrels GE, Clift PD, Pavlis TL, Draut AE (2007) U–Pb geochronology of volcanic rocks from the Jurassic Talkeetna Formation and detrital zircons from pre-arc and post-arc sequences: implications for the age of magmatism and inheritance in the Talkeetna arc. Geol Soc Am Spec Pap 431:253–271

Arai S, Ishimaru S (2008) Insights into petrological characteristics of the lithosphere of mantle wedge beneath arcs through peridotite xenoliths: a review. J Petrol 49(4):665–695

Arculus RJ (1994) Aspects of magma genesis in arcs. Lithos 33(1–3):189–208

Armstrong JT (1995) Citzaf-a package of correction programs for the quantitative electron microbeam X-ray-analysis of thick polished materials, thin-films, and particles. Microbeam Anal 4(3):177–200

Bacon CR, Bruggman PE, Christiansen RL, Clynne MA, Donnelly-Nolan JM, Hildreth W (1997) Primitive magmas at five Cascades volcanic fields: melts from hot, heterogeneous sub-arc mantle. Can Mineral 35:397–424

Ballhaus C (1993) Redox states of lithospheric and asthenospheric upper mantle. Contrib Mineral Petrol 114(3):331–348

Ballhaus C, Berry RF, Green DH (1991) High pressure experimental calibration of the olivine-orthopyroxene-spinel oxygen geobarometer: implications for the oxidation state of the upper mantle. Contrib Mineral Petrol 107(1):27–40

Barker F, Grantz A (1986) Talkeetna Formation in the south-eastern Talkeetna Mountains, southern Alaska: an Early Jurassic andesitic island arc. Geol Soc Am Abstr Progr 14:147

Barker F, Aleinikoff JN, Box S, Evans BW, Gehrels G, Hill MD, Irving AJ, Kelley JS, Leeman WP, Lull JS, Nockleberg WJ, Pallister JS, Patrick PE, Plafker G, Rubin CM (1994) Some accreted volcanic rocks of Alaska and their elemental abundances. In: Plafker G, Berg HC (eds) The geology of Alaska: Boulder, Colorado, Geological Society of America, Geology of North America, vol G-1, Geological Society of America, Boulder, CO, pp 555–587

Barsdell M, Smith IE (1989) Petrology of recrystallized ultramafic xenoliths from Merelava volcano, Vanuatu. Contrib Miner Petrol 102(2):230–241

Behn MD, Kelemen PB (2006) Stability of arc lower crust: insights from the Talkeetna arc section, south central Alaska, and the seismic structure of modern arcs. J Geophys Res Solid Earth 111:B11

Bell BR, Claydon RV (1992) The cumulus and post-cumulus evolution of chrome-spinels in ultrabasic layered intrusions: evidence from the Cuillin Igneous Complex, Isle of Skye, Scotland. Contrib Mineral Petrol 112(2–3):242–253

Berman RG (1988) Internally-consistent thermodynamic data for minerals in the system Na_2O-K_2O-CaO-MgO-FeO-Fe_2O_3-Al_2O_3-SiO_2-TiO_2-H_2O-CO_2. J petrol 29(2):445–522

Berry AJ, Stewart GA, O'Neill HSC, Mallmann G, Mosselmans JFW (2018) A re-assessment of the oxidation state of iron in MORB glasses. Earth Planet Sci Lett 483:114–123

Beyer BJ (1980) Petrology and geochemistry of ophiolite fragments in a tectonic mélange, Kodiak islands, Alaska, Ph.D. thesis, 227, University of California, Santa Cruz

Bézos A, Humler E (2005) The $Fe^{3+}/\Sigma Fe$ ratios of MORB glasses and their implications for mantle melting. Geochim Cosmochim Acta 69(3):711–725

Birner SK, Warren JM, Cottrell E, Davis FA (2016) Hydrothermal alteration of seafloor peridotites does not influence oxygen fugacity recorded by spinel oxybarometry. Geology 44(7):535–538

Birner SK, Cottrell E, Warren JM, Kelley KA, Davis FA (2018) Peridotites and basalts reveal broad congruence between two independent records of mantle f_{O2} despite local redox heterogeneity. Earth Planet Sci Lett 494:172–189

Blatter DL, Carmichael IS (1998) Hornblende peridotite xenoliths from central Mexico reveal the highly oxidized nature of subarc upper mantle. Geology 26(11):1035–1038

Bottinga Y, Allegre C (1976) Geophysical, petrological and geochemical models of the oceanic lithosphere. Tectonophysics 32(1–2):9–59

Brandon AD, Draper DS (1996) Constraints on the origin of the oxidation state of mantle overlying subduction zones: an example from Simcoe, Washington, USA. Geochim Cosmochim Acta 60(10):1739–1749

Brounce MN, Kelley KA, Cottrell E (2014) Variations in $Fe^{3+}/\sum Fe$ of Mariana arc basalts and mantle wedge fO_2. J Petrol 55(12):2513–2536

Bryant JA, Yogodzinski GM, Churikova TG (2007) Melt-mantle interactions beneath the Kamchatka arc: evidence from ultramafic xenoliths from Shiveluch volcano. Geochem Geophys Geosyst 8(4):1–24. https://doi.org/10.1029/2006GC001443

Bryndzia LT, Wood BJ (1990) Oxygen thermobarometry of abyssal spinel peridotites: the redox state and C–O–H volatile composition of the Earth's sub-oceanic upper mantle. Am J Sci 290(10):1093–1116

Burns LE (1985) The Border Ranges ultramafic and mafic complex, south-central Alaska: cumulate fractionates of island-arc volcanics. Can J Earth Sci 22(7):1020–1038

Burns LE, Pessel GH, Little TA, Pavlis TL, Newberry RJ, Winkler GR, Decker J (1991) Geology of the northern Chugach Mountains, south-central Alaska: Alaska Division of Geological and Geophysical Surveys Professional Report 94

Cameron EN (1975) Postcumulus and subsolidus equilibration of chromite and coexisting silicates in the eastern Bushveld complex. Geochim Cosmochim Acta 39:1021–1033

Canil D (1997) Vanadium partitioning and the oxidation state of Archaean komatiite magmas. Nature 389(6653):842–845

Canil D (2002) Vanadium in peridotites, mantle redox and tectonic environments: archean to present. Earth Planet Sci Lett 195(1–2):75–90

Canil D, O'Neill HSC (1996) Distribution of ferric iron in some upper-mantle assemblages. J Petrol 37(3):609–635

Canil D, Fedortchouk Y (2000) Clinopyroxene-liquid partitioning for vanadium and the oxygen fugacity during formation of cratonic and oceanic mantle lithosphere. J Geophys Res Solid Earth 105(B11):26003–26016

Canil D, O'Neill HSC, Pearson DG, Rudnick RL, McDonough WF, Carswell DA (1994) Ferric iron in peridotites and mantle oxidation states. Earth Planet Sci Lett 123(1–3):205–220

Carmichael ISE (1991) The redox states of basic and silicic magmas: a reflection of their source regions? Contrib Mineral Petrol 106(2):129–141

Carmichael IS, Ghiorso MS (1990) The effect of oxygen fugacity on the redox state of natural liquids and their crystallizing phases. Rev Min Geochem 24(1):191–212

Carmichael ISE, Nicholls JT, Smith AL (1970) Silica activity in igneous rocks. Am Min 55(1–2):246–263

Christie DM, Carmichael IS, Langmuir CH (1986) Oxidation states of mid-ocean ridge basalt glasses. Earth Planet Sci Lett 79(3–4):397–411

Clark SH (1972) The Wolverine complex, a newly discovered layered ultramafic body in the western Chugach Mountains, Alaska. USGS open-file report 72-70

Clark T (1978) Oxide minerals in the Turnagain ultramafic complex, northwestern British Columbia. Can J Earth Sci 15(12):1893–1903

Clift PD, Draut AE, Kelemen PB, Blusztajn J, Greene A (2005) Stratigraphic and geochemical evolution of an oceanic arc upper crustal section: the Jurassic Talkeetna Volcanic Formation, south-central Alaska. Geol Soc Am Bull 117(7–8):902–925

Coogan LA, Jenkin GR, Wilson RN (2002) Constraining the cooling rate of the lower oceanic crust: a new approach applied to the Oman ophiolite. Earth Planet Sci Lett 199(1–2):127–146

Cottrell E, Kelley KA (2011) The oxidation state of Fe in MORB glasses and the oxygen fugacity of the upper mantle. Earth Planet Sci Lett 305(3–4):270–282

Dalton JA, Lane SJ (1996) Electron microprobe analysis of Ca in olivine close to grain boundaries: the problem of secondary X-ray fluorescence. Am Min 81(1–2):194–201

Dauphas N, Craddock PR, Asimow PD, Bennett VC, Nutman AP, Ohnenstetter D (2009) Iron isotopes may reveal the redox conditions of mantle melting from Archean to Present. Earth Planet Sci Lett 288(1–2):255–267

Davis FA, Cottrell E, Birner SK, Warren JM, Lopez OG (2017) Revisiting the electron microprobe method of spinel-olivine-orthopyroxene oxybarometry applied to spinel peridotites. Am Mineral 102(2):421–435

DeBari SM, Coleman RG (1989) Examination of the deep levels of an island arc: evidence from the Tonsina ultramafic-mafic assemblage, Tonsina, Alaska. J Geophys Res Solid Earth 94(B4):4373–4391

DeBari SM, Greene AR (2011) Vertical stratification of composition, density, and inferred magmatic processes in exposed arc crustal sections. Arc-continent collision. Springer, Berlin, pp 121–144

Debari SM, Sleep NH (1991) High-Mg, low-Al bulk composition of the Talkeetna island arc, Alaska: implications for primary magmas and the nature of arc crust. Geol Soc Am Bull 103(1):37–47

Dick HJ, Bullen T (1984) Chromian spinel as a petrogenetic indicator in abyssal and alpine-type peridotites and spatially associated lavas. Contrib Miner Petrol 86(1):54–76

Dodson MH (1973) Closure temperature in cooling geochronological and petrological systems. Contrib Mineral Petrol 40(3):259–274

Dohmen R, Faak K, Blundy JD (2017) Chronometry and speedometry of magmatic processes using chemical diffusion in olivine, plagioclase and pyroxenes. Rev Mineral Geochem 83(1):535–575

Evans KA, Elburg MA, Kamenetsky VS (2012) Oxidation state of subarc mantle. Geology 40(9):783–786

Gaetani GA (2016) The behavior of Fe3+/Σ Fe during partial melting of spinel lherzolite. Geochimica et cosmochimica Acta 185:64–77

Greene AR, Debari SM, Kelemen PB, Blusztajn J, Clift PD (2006) A detailed geochemical study of island arc crust: the Talkeetna arc section, south-central Alaska. J Petrol 47(6):1051–1093

Grove T, Parman S, Bowring S, Price R, Baker M (2002) The role of an H_2O-rich fluid component in the generation of primitive basaltic andesites and andesites from the Mt. Shasta region, N California. Contrib Mineral Petrol 142(4):375–396

Hacker BR, Mehl L, Kelemen PB, Rioux M, Behn MD, Luffi P (2008) Reconstruction of the Talkeetna intraoceanic arc of Alaska through thermobarometry. J Geophys Res 113:B03204. https://doi.org/10.1029/2007JB005208

Hacker BR, Kelemen PB, Rioux M, McWilliams MO, Gans PB, Reiners PW, Layer PW, Söderlund U, Vervoort JD (2011) Thermochronology of the Talkeetna intraoceanic arc of Alaska: Ar/Ar, U-Th/He, Sm–Nd, and Lu–Hf dating. Tectonics 30(1):TC1011. https://doi.org/10.1029/2010TC002798

Henderson P (1970) The significance of the mesostasis of basic layered igneous rocks. J Petrol 11(3):463–473

Hirschmann MM (1991) Thermodynamics of multicomponent olivines and the solution properties of (Ni, Mg, Fe)$_2SiO_4$ and (Ca, Mg, Fe)$_2SiO_4$ olivines. Am Mineral 76:1232–1248

Holness MB, Vukmanovic Z, Mariani E (2017) Assessing the role of compaction in the formation of adcumulates: a microstructural perspective. J Petrol 58(4):643–673

Humphreys MC (2009) Chemical evolution of intercumulus liquid, as recorded in plagioclase overgrowth rims from the Skaergaard intrusion. J Petrol 50(1):127–145

Jackson ED (1961) Primary textures and mineral associations in the ultramafic zone of the Stillwater Complex, Montana. Prof Pap US Geol Surv 358:1–106

Jagoutz OE (2010) Construction of the granitoid crust of an island arc. Part II: a quantitative petrogenetic model. Contrib Mineral Petrol 160(3):359–381

Jagoutz O, Kelemen PB (2015) Role of arc processes in the formation of continental crust. Ann Rev Earth Planet Sci 43:363–404

Jull M, Kelemen PA (2001) On the conditions for lower crustal convective instability. J Geophys Res: Solid Earth 106(B4):6423–6446

Jurewicz AJ, Watson EB (1988) Cations in olivine, part 2: diffusion in olivine xenocrysts, with applications to petrology and mineral physics. Contrib Mineral Petrol 99(2):186–201

Kelemen PB, Hanghøj K, Greene AR (2003) One view of the geochemistry of subduction-related magmatic arcs, with an emphasis on primitive andesite and lower crust. In: Rudnick RL (ed) The Crust. Elsevier, New York, pp 593–659

Kelemen PB, Hanghøj K, Greene A (2014) One view of the geochemistry of subduction-related magmatic arcs, with an emphasis on primitive andesite and lower crust. In: Rudnick RL (ed) Treatise on geochemistry, vol 4: the crust, 2nd edn. Pergamon, Oxford, pp 746–805

Kelley KA, Cottrell E (2009) Water and the oxidation state of subduction zone magmas. Science 325(5940):605–607

Kelley KA, Cottrell E (2012) The influence of magmatic differentiation on the oxidation state of Fe in a basaltic arc magma. Earth Planet Sci Lett 329:109–121

Kelley KA, Plank T, Grove TL, Stolper EM, Newman S, Hauri E (2006) Mantle melting as a function of water content beneath back-arc basins. J Geophys Res 111:B09208. https://doi.org/10.1029/2005JB003732

Kerr RC, Tait SR (1986) Crystallization and compositional convection in a porous medium with application to layered igneous intrusions. J Geophys Res Solid Earth 91(B3):3591–3608

Kinzler RJ (1997) Melting of mantle peridotite at pressures approaching the spinel to garnet transition: application to mid-ocean ridge basalt petrogenesis. J Geophys Res Solid Earth 102(B1):853–874

Köhler TP, Brey G (1990) Calcium exchange between olivine and clinopyroxene calibrated as a geothermobarometer for natural peridotites from 2 to 60 kb with applications. Geochim Cosmochim Acta 54(9):2375–2388

Kress VC, Carmichael IS (1991) The compressibility of silicate liquids containing Fe_2O_3 and the effect of composition, temperature, oxygen fugacity and pressure on their redox states. Contrib Mineral Petrol 108(1–2):82–92

Kusky TM, Glass A, Tucker R (2007) Structure, Cr-chemistry, and age of the border ranges Ultramafic–Mafic complex: a suprasubduction zone ophiolite complex. Geol Soc Am Spec Pap 431:207

Laubier M, Grove TL, Langmuir CH (2014) Trace element mineral/melt partitioning for basaltic and basaltic andesitic melts: an experimental and laser ICP-MS study with application to the oxidation state of mantle source regions. Earth Planet Sci Lett 392:265–278

Lee CTA, Leeman WP, Canil D, Li ZXA (2005) Similar V/Sc systematics in MORB and arc basalts: implications for the oxygen fugacities of their mantle source regions. J Petrol 46(11):2313–2336

Lee CTA, Luffi P, Le Roux V, Dasgupta R, Albaréde F, Leeman WP (2010) The redox state of arc mantle using Zn/Fe systematics. Nature 468(7324):681–685

Lee CTA, Luffi P, Chin EJ, Bouchet R, Dasgupta R, Morton DM, Le Roux V, Yin QZ, Jin D (2012) Copper systematics in arc magmas and implications for crust-mantle differentiation. Science 336(6077):64–68

Li ZXA, Lee CTA (2004) The constancy of upper mantle fO_2 through time inferred from V/Sc ratios in basalts. Earth Planet Sci Lett 228(3–4):483–493

Li J, Kornprobst J, Vielzeuf D, Fabriès J (1995) An improved experimental calibration of the olivine-spinel geothermometer. Chin J Geochem 14(1):68–77

Lindsley DH, Frost BR (1992) Equilibria among Fe–Ti oxides, pyroxenes, olivine, and quartz: part I. Theory. Am Mineral 77(9–10):987–1003

Mallmann G, O'Neill HSC (2009) The crystal/melt partitioning of V during mantle melting as a function of oxygen fugacity compared with some other elements (Al, P, Ca, Sc, Ti, Cr, Fe, Ga, Y, Zr and Nb). J Petrol 50(9):1765–1794

Mallmann G, O'Neill HSC (2013) Calibration of an empirical thermometer and oxybarometer based on the partitioning of Sc, Y and V between olivine and silicate melt. J Petrol 54(5):933–949

Markl G, Marks M, Wirth R (2001) The influence of T, $aSiO_2$, and fO_2 on exsolution textures in Fe–Mg olivine: an example from augite syenites of the Ilimaussaq Intrusion, South Greenland. Am Mineral 86(1–2):36–46

Mattioli GS, Wood BJ (1988) Magnetite activities across the $MgAl_2O_4$–Fe_3O_4 spinel join, with application to thermobarometric estimates of upper mantle oxygen fugacity. Contrib Mineral Petrol 98(2):148–162

Mehl L, Hacker BR, Hirth G, Kelemen PB (2003) Arc-parallel flow within the mantle wedge: Evidence from the accreted Talkeetna arc, south central Alaska. J Geophys Res. https://doi.org/10.1029/2002jb002233

Moore JG, Evans BW (1967) The role of olivine in the crystallization of the prehistoric Makaopuhi tholeiitic lava lake, Hawaii. Contrib Mineral Petrol 15(3):202–223

Nandedkar RH, Ulmer P, Müntener O (2014) Fractional crystallization of primitive, hydrous arc magmas: an experimental study at 0.7 GPa. Contrib Mineral Petrol 167(6):1015

Nebel O, Sossi PA, Benard A, Wille M, Vroon PZ, Arculus RJ (2015) Redox-variability and controls in subduction zones from an iron-isotope perspective. Earth Planet Sci Lett 432:142–151

Newberry RJ, Burns LE, Pessel GH (1986) Volcanogenic massive sulfide deposits and the "missing complement" to the calc-alkaline trend; evidence from the Jurassic Talkeetna island arc of southern Alaska. Econ Geol 81(4):951–960

Niu Y (2004) Bulk-rock major and trace element compositions of abyssal peridotites: implications for mantle melting, melt extraction and post-melting processes beneath mid-ocean ridges. J Petrol 45(12):2423–2458

Osborn EF (1959) Role of oxygen pressure in the crystallization and differentiation of basaltic magma. Am J Sci 257(9):609–647

Parkinson IJ, Arculus RJ (1999) The redox state of subduction zones: insights from arc-peridotites. Chem Geol 160(4):409–423

Parkinson IJ, Pearce JA (1998) Peridotites from the Izu–Bonin–Mariana forearc (ODP Leg 125): evidence for mantle melting and melt–mantle interaction in a supra-subduction zone setting. J Petrol 39(9):1577–1618

Parkinson IJ, Arculus RJ, Eggins SM (2003) Peridotite xenoliths from Grenada, Lesser Antilles island arc. Contrib Mineral Petrol 146(2):241–262

Pavlis TL (1982) Origin and age of the Border Ranges fault of southern Alaska and its bearing on the late Mesozoic tectonic evolution of Alaska. Tectonics 1(4):343–368

Pavlis TL (1983) Pre-Cretaceous crystalline rocks of the western Chugach Mountains, Alaska: nature of the basement of the Jurassic Peninsular terrane. Geol Soc Am Bull 94:1329–1344

Plafker G, Nokleberg WJ, Lull JS (1989) Bedrock geology and tectonic evolution of the Wrangellia, Peninsular, and Chugach terranes along the Trans-Alaska Crustal Transect in the Chugach Mountains and southern Copper River Basin, Alaska. J Geophys Res Solid Earth 94(B4):4255–4295

Presnall DC (1966) The join forsterite-diopside-iron oxide and its bearing on the crystallization of basaltic and ultramafic magmas. Am J Sci 264(10):753–809

Prytulak J, Sossi PA, Halliday AN, Plank T, Savage PS, Woodhead JD (2017) Stable vanadium isotopes as a redox proxy in magmatic systems? Geochem Perspect Lett 3(1):75–84

Putirka KD (2008) Thermometers and barometers for volcanic systems. Rev Mineral Geochem 69(1):61–120

Richards JP (2015) The oxidation state, and sulfur and Cu contents of arc magmas: implications for metallogeny. Lithos 233:27–45

Rioux M, Hacker B, Mattinson J, Kelemen P, Blusztajn J, Gehrels G (2007) Magmatic development of an intra-oceanic arc: high-precision U–Pb zircon and whole-rock isotopic analyses from the accreted Talkeetna arc, south-central Alaska. Geol Soc Am Bull 119(9–10):1168–1184

Rioux M, Mattinson J, Hacker B, Kelemen P, Blusztajn J, Hanghøj K, Gehrels G (2010) Intermediate to felsic middle crust in the accreted Talkeetna arc, the Alaska Peninsula and Kodiak Island, Alaska: an analogue for low-velocity middle crust in modern arcs. Tectonics 29(3):TC3001. https://doi.org/10.1029/2009TC002541

Roeder PL, Campbell IH (1985) The effect of postcumulus reactions on composition of chrome-spinels from the Jimberlana intrusion. J Petrol 26(3):763–786

Rose AW (1966) Geology of chromite-bearing ultramafic rocks near Eklutna, Anchorage Quadrangle, Alaska. Alaska Division of Mines and Minerals. Geologic report 18, 1 sheet, scale 1:63,360

Sack RO, Ghiorso MS (1991a) An internally consistent model for the thermodynamic properties of Fe–Mg–titanomagnetite–aluminate spinels. Contrib Mineral Petrol 106:474–505

Sack RO, Ghiorso MS (1991b) Chromian spinels as petrogenetic indicators: thermodynamic and petrologic applications. Am Mineral 76:827–847

Sack RO, Ghiorso MS (1994a) Thermodynamics of multicomponent pyroxenes I. Formulation of general model. Contrib Mineral Petrol 116:277–286

Sack RO, Ghiorso MS (1994b) Thermodynamics of multicomponent pyroxenes II. Applications to phase relations in the quadrilateral. Contrib Mineral Petrol 116:287–300

Sack RO, Ghiorso MS (1994c) Thermodynamics of multicomponent pyroxenes III. Calibration of $Fe^{2+}(Mg)_{-1}$, $TiAl(MgSi)_{-1}$, $TiFe^{3+}(MgSi)_{-1}$, $AlFe^{3+}(MgSi)_{-1}$, $NaAl(CaMg)_{-1}$, $Al_2(MgSi)_{-1}$, and $Ca(Mg)_{-1}$ exchange reactions between pyroxenes and silicate melts. Contrib Mineral Petrol 118:271–296

Sato M (1978) Oxygen fugacity of basaltic magmas and the role of gas-forming elements. Geophys Res Lett 5(6):447–449

Shaw DM (1970) Trace element fractionation during anatexis. Geochimica et Cosmochimica Acta 34(2):237–243

Shejwalkar A, Coogan LA (2013) Experimental calibration of the roles of temperature and composition in the Ca-in-olivine geothermometer at 0.1 MPa. Lithos 177:54–60

Shervais JW (1982) Ti–V plots and the petrogenesis of modern and ophiolitic lavas. Earth Planet Sci Lett 59(1):101–118

Simkin T, Smith JV (1970) Minor-element distribution in olivine. J Geol 78(3):304–325

Sisson TW, Ratajeski K, Hankins WB, Glazner AF (2005) Voluminous granitic magmas from common basaltic sources. Contrib Mineral Petrol 148(6):635–661

Sisson TW, Kimura JI, Coombs ML (2009) Basanite–nephelinite suite from early Kilauea: carbonated melts of phlogopite–garnet peridotite at Hawaii's leading magmatic edge. Contrib Mineral Petrol 158(6):803

Sparks RSJ, Huppert HE, Kerr RC, McKenzie DP, Tait SR (1985) Postcumulus processes in layered intrusions. Geol Mag 122(5):555–568

Stolper DA, Bucholz CE (2019) A Neoproterozoic to early Phanerozoic rise in island arc redox state due to deep ocean oxygenation and increased marine sulfate levels. Proc Natl Acad Sci 116(18):8746–8755

Stolper E, Newman S (1994) The role of water in the petrogenesis of Mariana trough magmas. Earth Planet Sci Lett 121(3–4):293–325

Stormer JC Jr (1973) Calcium zoning in olivine and its relationship to silica activity and pressure. Geochimica et Cosmochimica Acta 37(8):1815–1821

Tait SR, Jaupart C (1992) Compositional convection in a reactive crystalline mush and melt differentiation. J Geophys Res Solid Earth 97(B5):6735–6756

Tait SR, Huppert HE, Sparks RSJ (1984) The role of compositional convection in the formation of adcumulate rocks. Lithos 17:139–146

Tang M, Erdman M, Eldridge G, Lee CTA (2018) The redox "filter" beneath magmatic orogens and the formation of continental crust. Sci Adv 4(5):eaar4444

Toth MI (1981) Petrology, geochemistry, and origin of the Red Mountain ultramafic body near Seldovia, Alaska. USGS open-file report 81-514

Ulmer P, Kaegi R, Müntener O (2018) Experimentally derived intermediate to silica-rich arc magmas by fractional and equilibrium crystallization at 1.0 GPa: an evaluation of phase relationships, compositions, liquid lines of descent and oxygen fugacity. J Petrol 59(1):11–58

Van Orman JA, Crispin KL (2010) Diffusion in oxides. Rev Mineral Geochem 72(1):757–825

VanTongeren JA, Kelemen PB, Hanghøj K (2008) Cooling rates in the lower crust of the Oman ophiolite: Ca in olivine, revisited. Earth Planet Sci Lett 267(1–2):69–82

Voigt M, von der Handt A (2011) Influence of subsolidus processes on the chromium number in spinel in ultramafic rocks. Contrib Mineral Petrol 162(4):675–689

Wager LR, Brown GM, Wadsworth WJ (1960) Types of igneous cumulates. J Petrol 1(1):73–85

Wang J, Xiong X, Takahashi E, Zhang L, Li L, Liu X (2019) Oxidation state of arc mantle revealed by partitioning of V, Sc, and Ti between mantle minerals and basaltic melts. J Geophys Res. https://doi.org/10.1029/2018JB016731

Warren JM (2016) Global variations in abyssal peridotite compositions. Lithos 248:193–219

Williams HM, McCammon CA, Peslier AH, Halliday AN, Teutsch N, Levasseur S, Burg JP (2004) Iron isotope fractionation and the oxygen fugacity of the mantle. Science 304(5677):1656–1659

Williams HM, Peslier AH, McCammon C, Halliday AN, Levasseur S, Teutsch N, Burg JP (2005) Systematic iron isotope variations in mantle rocks and minerals: the effects of partial melting and oxygen fugacity. Earth Planet Sci Lett 235(1–2):435–452

Wilson AH (1982) The geology of the Great 'Dyke', Zimbabwe: the ultramafic rocks. J Petrol 23(2):240–292

Wilson FH, Hults CP, Mull CG, Karl SM (2015) Geologic map of Alaska: U.S. Geological Survey Scientific Investigations Map 3340, pamphlet 196 p., 2 sheets, scale 1:1,584,000. http://dx.doi.org/10.3133/sim3340

Wood BJ (1990) An experimental test of the spinel peridotite oxygen barometer. J Geophys Res Solid Earth 95(B10):15845–15851

Wood BJ, Virgo D (1989) Upper mantle oxidation state: ferric iron contents of lherzolite spinels by ^{57}Fe Mössbauer spectroscopy and resultant oxygen fugacities. Geochim Cosmochim Acta 53(6):1277–1291

Woodhead J, Eggins S, Gamble J (1993) High field strength and transition element systematics in island arc and back-arc basin basalts: evidence for multi-phase melt extraction and a depleted mantle wedge. Earth Planet Sci Lett 114(4):491–504

Woodland AB, Kornprobst J, Wood BJ (1992) Oxygen thermobarometry of orogenic lherzolite massifs. J Petrol 33(1):203–230

Woodland AB, Kornprobst J, McPherson E, Bodinier JL, Menzies MA (1996) Metasomatic interactions in the lithospheric mantle: petrologic evidence from the Lherz massif, French Pyrenees. Chem Geol 134(1–3):83–112

Woodland AB, Kornprobst J, Tabit A (2006) Ferric iron in orogenic lherzolite massifs and controls of oxygen fugacity in the upper mantle. Lithos 89(1–2):222–241

Zhang HL, Cottrell E, Solheid PA, Kelley KA, Hirschmann MM (2018) Determination of $Fe^{3+}/\Sigma Fe$ of XANES basaltic glass standards by Mössbauer spectroscopy and its application to the oxidation state of iron in MORB. Chem Geol 479:166–175